JGR Solid Earth

RESEARCH ARTICLE
10.1029/2024JB031081

Channeling, Clogging and Permeability Oscillations: Different Macroscopic Regimes in Mineral Replacement

Agnieszka Budek[1] **and Piotr Szymczak**[1]

[1]Faculty of Physics, Institute of Theoretical Physics, University of Warsaw, Warsaw, Poland

Key Points:

- The interplay of dissolution and precipitation can give rise to spatially inhomogeneous patterns
- These patterns fill the space uniformly, efficiently distributing the secondary phase throughout the system
- Permeability of the system oscillates, as new flowpaths emerge only to be subsequently blocked by precipitate

Supporting Information:

Supporting Information may be found in the online version of this article.

Correspondence to:

P. Szymczak,
piotrek@fuw.edu.pl

Citation:

Budek, A., & Szymczak, P. (2025). Channeling, clogging and permeability oscillations: Different macroscopic regimes in mineral replacement. *Journal of Geophysical Research: Solid Earth*, *130*, e2024JB031081. https://doi.org/10.1029/2024JB031081

Received 19 JAN 2025
Accepted 24 APR 2025

Author Contributions:

Conceptualization: Agnieszka Budek, Piotr Szymczak
Data curation: Agnieszka Budek, Piotr Szymczak
Formal analysis: Agnieszka Budek, Piotr Szymczak
Funding acquisition: Piotr Szymczak
Investigation: Agnieszka Budek, Piotr Szymczak
Methodology: Agnieszka Budek, Piotr Szymczak
Resources: Piotr Szymczak
Software: Agnieszka Budek
Validation: Agnieszka Budek
Visualization: Agnieszka Budek
Writing – original draft: Agnieszka Budek, Piotr Szymczak
Writing – review & editing: Agnieszka Budek, Piotr Szymczak

Abstract We consider a porous medium infiltrated by a reactive fluid which triggers coupled dissolution-precipitation reactions at pore surfaces. To study these processes, we model the medium as a system of interconnected pipes with the diameter of each segment changing in proportion to the local reactant consumption. With this model, we investigate different growth regimes in an evolving porous medium, allowing for both erosion and precipitation of the dissolved material. The interplay of flow, transport and reaction in such a system can give rise to a variety of patterns: from spontaneous channeling to nearly homogeneous transformation of the entire rock matrix into the product phase. Interestingly, even if the product phase has a larger molar volume than the parent phase, clogging in such a system can be avoided, due to the interplay of dissolution and precipitation resulting in the continuous creation of new flow paths. These results can be relevant for the analysis of carbonation reactions, in which an important goal is to avoid clogging of the pore space that can lead to permeability reduction and the overall slowdown of the process.

Plain Language Summary In this study, we explore how fluids moving through rocks can dissolve minerals and deposit new ones, changing the rock's structure. This process can either create pathways that allow fluids to flow more easily or block these pathways, making the rock more compact. We use a numerical model to simulate a network of pores within the rock, observing how different conditions affect the formation of new channels or the blocking of existing ones. Our findings show that the outcome—whether the rock becomes more open or more clogged—depends on the balance between the mineral being dissolved and the new mineral being formed. Factors like the size of the mineral particles, how fast they dissolve or form, and the initial structure of the rock all play a crucial role. Understanding and controlling these conditions can help in applications like mineral carbonation, where maintaining fluid flow in rocks is essential.

1. Introduction

Dissolution, precipitation, and chemical reactions between solutes and solids may gradually alter the composition and structure of the solid matrix, either creating or destroying permeable paths for fluid flow. Complex, dynamic feedback thus arises where, on the one hand, the fluid flow affects the characteristics of the solid medium, and on the other hand the changing medium influences the fluid flow. Such feedback between the flow of fluids and the media in which they flow are important for understanding the slow processes, which—over geological timescales—may transform the rock masses (Korzhinskii, 1968; P. J. Ortoleva, 1994). Among these reactive processes, it is commonly encountered that a secondary mineral precipitates when a primary mineral dissolves, and the precipitation and dissolution reactions are closely coupled with each other (Korzhinskii, 1968; Putnis, 2021). A classic example of this kind is dolomitization (Merino & Canals, 2011), in which vast rock masses of limestone are transformed into dolomite by the dissolution of calcite followed by dolomite precipitation, silicification (replacement of minerals by silica) (Bustillo, 2010), or serpentinization (replacement of Fe–Mg silicates by serpentine minerals) (Barnes & O'Neil, 1978; Wicks & Whittaker, 1977). Understanding of the dissolution/precipitation processes is also crucial for such applications as sustaining the fluid circulation in geothermal systems (Wagner et al., 2005), the long-term geochemical evolution of host rock in nuclear waste repositories (De Windt et al., 2004) or the creation of subsurface barriers to mitigate the spread of contaminants in groundwater (A. Cohen et al., 2021). Another important application is the mineral trapping of carbon dioxide (Matter & Kelemen, 2009; Oelkers et al., 2008)—here the primary silicate mineral dissolves due to a decrease of pH caused by the presence of aqueous CO_2; meanwhile, CO_2 reacts with cations released by the dissolution reaction to form a secondary precipitate of carbonate mineral. Mineral carbonation provides a permanent and safe way for storing carbon dioxide, which is compelling due to the need for large scale cost-effective means to reduce the carbon content in the atmosphere and oceans to mitigate global warming effects.

If the system undergoes dissolution only, the reaction front is often destabilized. Even if the front is initially planar, small perturbations emerge, which absorb more flow and amplify into finger-like or funnel-like structures, such as wormholes or solution pipes (Daccord & Lenormand, 1987; Hoefner & Fogler, 1988; Lipar et al., 2021). This mechanism is referred to in the literature as the *reactive-infiltration instability* (Aharonov et al., 1995; Chadam et al., 1986; Hinch & Bhatt, 1990). Networks of caves and sinkholes are formed by the dissolution of limestone by CO_2-enriched water in karst areas (Palmer, 1991; Szymczak & Ladd, 2011), the ascending magma dissolves the peridotite rocks, leading to formation of a network of high-permeability channels (Aharonov et al., 1995; Daines & Kohlstedt, 1994; Kelemen et al., 1995; Spiegelman et al., 2001), matrix acidizing is used by petroleum engineers to enlarge the natural pores of the reservoirs (Rowan, 1959)—in all these processes, the interplay of flow and reaction in an evolving geometry results in the spontaneous formation of intricate patterns. Flow-induced dissolution, characterized by strong, nonlinear coupling between transport and geometry evolution have been investigated in numerous experimental (Al-Khulaifi et al., 2019; Daccord, 1987; Daccord & Lenormand, 1987; Hoefner & Fogler, 1988; Li et al., 2019; Luquot & Gouze, 2009; Menke et al., 2018; Ott & Oedai, 2015; Snippe et al., 2020) and theoretical (C. Cohen et al., 2008; Golfier et al., 2002; Panga et al., 2005; Steefel & Lasaga, 1990; Szymczak & Ladd, 2009; Soulaine et al., 2017) studies, the latter often combined with numerical simulations.

On the other hand, precipitation reactions tend to stabilize the reaction front by decreasing the permeability of the rock (Woods, 2014). In this paper, we are concerned with the case where dissolution and precipitation coexist, linked by common ion(s). There are indications that such fronts can also become unstable, leading to fingering structures. Natural examples include the fingering of dolomitization fronts (Centrella et al., 2021; Koeshidayatullah et al., 2020; Merino & Canals, 2011) or the formation of uranium rolls, where uraninite precipitates at the redox front separating oxidized rock from reduced rock (Dewynne et al., 1993). Pattern formation in dissolution-precipitation systems has also been observed experimentally, such as in calcite dissolution coupled with ferric hydroxide (Rege & Fogler, 1989) or gypsum precipitation (Garcia-Rios et al., 2015; Singurindy & Berkowitz, 2003a, 2003b), and in the replacement of strontium sulfate by barium sulfate (Poonoosamy et al., 2015).

Although several theoretical studies of the instabilities in dissolution-precipitation fronts have been conducted (Banerjee & Merino, 2011; Beinlich et al., 2020; Kondratiuk et al., 2015, 2017; Korzhinskii, 1968), a thorough characterization of these systems is still missing. The obvious reason for this is the presence of a large number of controlling factors in such systems including infiltration rate, dissolution and precipitation reaction rates or molar volume of the primary and secondary phases. This complexity is precisely what makes the problem challenging and worthy of consideration.

2. Network Model

The main numerical tool used in this paper to investigate the chemical transformations in porous media will be a pore network model. We will draw on our prior experience with network models for exploring dissolution in evolving porous media (Budek & Szymczak, 2012; Roded et al., 2020, 2021; Sharma et al., 2023), extending this approach to include coupled dissolution-precipitation processes. Pore-network models offer a computationally efficient yet geometrically explicit framework that facilitates control over pore architecture—such as diameters, lengths, and connectivity—allowing one to adjust the network to represent different rock types. A key advantage of this approach is that it enables the resolution of pore-scale gradients in concentration, which are often homogenized in continuum models. This fine-scale resolution is essential for accurately modeling structure–flow–reaction feedbacks, which govern the emergence of features like wormholing and are central to reactive infiltration instability. As dissolution and precipitation modify the pore space, the network structure can be dynamically updated, allowing us to trace evolving permeability, transport properties, and effective reaction rates during chemical transformation of rocks (Ameri et al., 2017; Budek & Szymczak, 2012; Raoof et al., 2012; Varloteaux et al., 2013). This makes pore-network models a particularly useful tool for investigating the interplay between microstructure and macroscopic transport in reactive porous media.

In the network model, the medium is represented as a collection of connected capillaries with heterogeneous diameters that evolve through the dissolution and precipitation of mineral material, as illustrated in Figure 1. To obtain the volumetric flow in the network, a sparse system of linear equations needs to be solved to relate the pressure at each node to the volumetric flux q_{ij} in an individual capillary element (pore) connecting two nodes

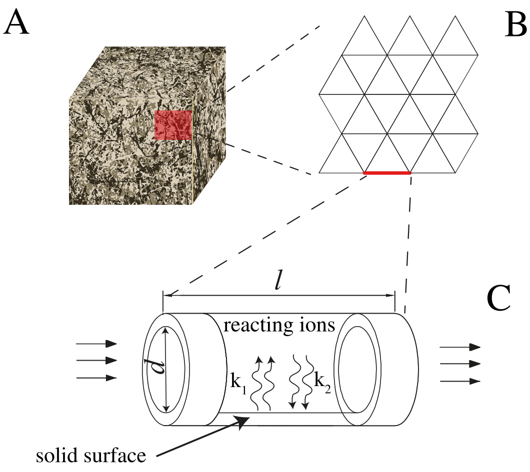

Figure 1. Schematic of the pore network model for tracking flow and geometry evolution in an evolving porous medium. The rock (a) is represented as a network of elementary pores (b), each characterized by a length, *l*, and diameter, *d*, which evolves in time due to the dissolution/precipitation reactions (c).

indexed by i and j. Each of these elements will be described in one-dimensional manner, assuming that the diameter is constant along its length. The link between the volumetric flow, q_{ij}, and the pressure drop along the pore is then given by

$$q_{ij} = -\frac{\pi}{128\mu l_{ij}} d_{ij}^4 (p_j - p_i), \tag{1}$$

where d_{ij} is the pore diameter and μ is the dynamic viscosity of the fluid. At each node, we also have a continuity condition, $\sum_i q_{ij} = 0$, where the sum is over all the nodes i connected by a pore with node j. The resulting system of sparse linear equations is then solved for the pressure values at the nodes by a linear algebra solver. To this end, we use the multi-frontal massively parallel solver (MUMPS) (Amestoy et al., 2001, 2006).

The concentration of reactive species c^k along each pore is found by solving the convection-reaction equation

$$\frac{\partial (q c^k)}{\partial x} = -\pi d R_k (c^1, \ldots, c^N), \tag{2}$$

where πd accounts for the reactive surface area (assumed to be equal to the lateral surface of the pore) and R is the reaction term involving, in principle, the concentrations of all reactive species.

By integrating Equation 2 along the pore, we can find the link between the concentrations of the reactive species at the inlet and outlet of each pore (Figure 2). This is supplemented by the solute balance equations at the pore intersections, which assume full mixing (Park et al., 2001; Sharma et al., 2023) that is, solute from inlet branches is assumed to mix instantaneously at the intersection, resulting in homogeneous concentrations in the outlet branches. The concentration of species k at a given node j with incoming pores ij is then determined by equation:

$$c_j^k = \frac{\sum_i q_{ij} c_{ij}^k}{\sum_i q_{ij}}, \tag{3}$$

where and c_{ij}^k is the outlet concentration of pore ij. Other mixing rules, such as streamline routing, can be considered (Sharma et al., 2023) and they might influence the dissolution patterns to some extent.

By combining mixing rules (Equation 3) with the integrated reaction-convection solutions (Equation 2), we obtain another sparse linear system, this time for the concentrations of reactive species at the lattice nodes. The local expansion of each pore element then follows in proportion to the dissolution and/or precipitation rate at each point. To keep the system mathematically tractable, an approximation is usually adopted in which the diameter of each pore element is assumed to be constant along its length. Consequently, the reactive flux is integrated along the pore, and the resulting dissolved/precipitated volume is uniformly distributed along its length (Budek & Szymczak, 2012; Hoefner & Fogler, 1988). Importantly, flow and transport equations do not include time derivatives, as we assume that the dissolution time-scales are much longer than the flow and transport relaxation

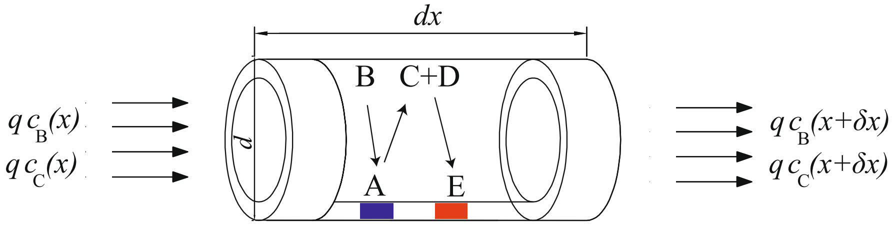

Figure 2. Reactions within the pore: dissolution: $A + B \rightarrow C_{\uparrow}$ and precipitation $C + D \rightarrow E_{\downarrow}$.

times. This assumption allows us to use the quasi-static approach, treating the flow and concentration fields as stationary at each time-step (Lichtner, 1988).

The reactive fluid enters from the upper edge, where pressure p_{in} is applied, and exits from the lower edge, where the pressure is $p_{\mathrm{out}} = 0$. In our study, we consider a scenario with a constant total flow through the system, thus at each time step, p_{in} is scaled accordingly. Additionally, periodic boundary conditions are applied along the lateral direction.

Additional details regarding the algorithm are provided in the following section, where we focus on implementing the network algorithm for a specific dissolution-precipitation system.

3. Dissolution-Precipitation

To get a first insight into the interplay of flow, transport and reactions in dissolution-precipitation systems, we consider the simplest dissolution-precipitation reaction, in which the dissolution of mineral *A* by reactant *B*

$$\text{reaction 1:}\quad \chi_A \mathrm{A} + \chi_B \mathrm{B} \rightarrow \mathrm{C}^{\uparrow}$$

is coupled by a common ion *C* with precipitation of mineral *E*,

$$\text{reaction 2:}\quad \mathrm{C} + \chi_D \mathrm{D} \rightarrow \chi_E \mathrm{E}_{\downarrow}$$

as depicted in Figure 2. Here χ_i are the stoichiometric coefficients for the reactions.

One example of such reactions is sandstone acidizing used to increase the permeability of sandstone oil reservoirs (Economides & Nolte, 2000). In this process hydrofluoric acid dissolves silica, releasing silicon hexafluoride ions into the solution. These ions react with sodium ions in the brine, forming sodium fluorosilicate that precipitates out of the solution:

$$\mathrm{SiO_2} + 6\mathrm{HF} \rightarrow \mathrm{SiF_6^{2-}} + 2\mathrm{H_2O} + 2\mathrm{H^+}$$
$$2\mathrm{Na^+} + \mathrm{SiF_6^{2-}} \rightarrow \mathrm{Na_2SiF_6}\downarrow.$$

A similar dissolution-precipitation coupling through a common ion is at the base of mineral carbonation processes (Andreani et al., 2009; Matter & Kelemen, 2009; Sanna et al., 2014). As an example, let us take the dissolution of forsterite coupled with precipitation of magnesite (Matter & Kelemen, 2009). To begin with, the carbon dioxide dissolves in water

$$\mathrm{CO_2(aq)} + \mathrm{H_2O} \rightarrow \mathrm{CO_3^{2-}} + 2\mathrm{H^+}.$$

The hydrogen ions produced in this reaction are then dissolving forsterite

$$\mathrm{Mg_2SiO_{4(s)}} + 4\mathrm{H^+} + \mathrm{H_2O} \rightarrow 2\mathrm{Mg^{2+}} + \mathrm{H_4SiO_4}.$$

In turn, magnesium ions released in this reaction are reacting with carbonate ions forming magnesite, which precipitates

$$\mathrm{Mg^{2+}} + \mathrm{CO_3^{2-}} \rightarrow \mathrm{MgCO_3(s)}.$$

One of the challenges here is to assess how to prevent self-clogging of this reaction under the conditions when the precipitated product (E) has an equal or larger molar volume than the dissolved mineral (A), as is the case in most of the mineral carbonation reactions.

The kinetics of water-rock interactions can be very complex (Lasaga, 1984). However, here, we assume reaction rates that are linear in concentrations of reactants to keep the model simple and focus more on the couplings between flow and porosity evolution rather than on the intricacies of the reactions:

$$R_{\text{diss}} = k_1 c_B, \qquad R_{\text{prec}} = k_2 c_C, \tag{4}$$

where we assumed that both reactions are irreversible, meaning that the corresponding back reactions can be neglected. Additionally, we assume that there is a large supply of D ions in the fluid; hence, their concentration does not limit the rate of the precipitation reaction.

The concentrations c_B and c_C in Equation 4 correspond to the ion concentration at the surface of the pores, where the reactions take place. These are, in general, lower than the bulk concentration due to the hindering role of the diffusion, particularly pronounced in wider pores. These effects can be taken into account by introducing the effective reaction rates (Szymczak & Ladd, 2009)

$$k_1^{\text{eff}}(d) = \frac{k_1}{1 + k_1 d / D_B \text{Sh}} \qquad k_2^{\text{eff}}(d) = \frac{k_2}{1 + k_2 d / D_C \text{Sh}}. \tag{5}$$

Here D is the diffusion coefficient of the reagent and Sh is the Sherwood number, which is the non-dimensional mass transfer coefficient (Bejan, 1984; Gupta & Balakotaiah, 2001) characterizing the magnitude of the diffusive current to the reactive wall.

The mass balance equations for B and C components, corresponding to the coupled reactions 1–2 take then the form:

$$q \delta c_B = -\chi_B \pi d R_{\text{diss}} = -\chi_B \pi d k_1^{\text{eff}} c_B \delta x, \tag{6}$$

$$q \delta c_C = \pi d R_{\text{diss}} - \pi d R_{\text{prec}} = \left(\pi d k_1^{\text{eff}} c_B\right) \delta x - \left(\pi d k_2^{\text{eff}} c_C\right) \delta x, \tag{7}$$

where δc_B and δc_C are the changes in B and C concentrations over the length δx (see Figure 2) and we assumed advection-dominated transport along the axial direction (x). Note that transverse diffusion effects are incorporated into the effective reaction coefficient, k^{eff} (Equation 5).

We can get rid of the stoichiometric coefficient χ_B in the above equations by rescaling the concentrations and reaction rates:

$$c_B' = \chi_B^{-1} c_B, \qquad k_1^{\text{eff}'} = \chi_B k_1^{\text{eff}}, \tag{8}$$

which corresponds to tracking χ_B ions of B species instead of a single ion. With this rescaling, after dropping the primes, Equation 6 takes the form

$$q \frac{dc_B}{dx} = -\left(\pi d k_1^{\text{eff}} c_B\right), \tag{9}$$

while Equation 7 retains its previous form.

For a channel of a uniform diameter, these equations can be integrated to yield

$$\begin{aligned} c_B(x) &= c_{B0} e^{-\text{Da}_1 x/l}, \\ c_C(x) &= c_{B0} \frac{\text{Da}_1}{\text{Da}_1 - \text{Da}_2} \left(e^{-\text{Da}_2 x/l} - e^{-\text{Da}_1 x/l}\right) + c_{C0} e^{-\text{Da}_2 x/l}, \end{aligned} \tag{10}$$

where c_{i0} denotes the concentration of reagent i at the inlet of a pore and we introduced a local, effective Damköhler number for reaction 1 and 2 as

$$\text{Da}_i(d,q) = \frac{\pi k_i^{\text{eff}}(d) l d}{q} = \frac{\pi k_i l d}{q(1 + k_i d / D_i \text{Sh})}, \tag{11}$$

which depends on the local flow rate and diameter of a given pore. The effective Damköhler number is related to the reactant penetration length, which will be discussed in detail in Section 5.

Given the reaction rates, the change of radii of the pores can be calculated based on the mass conservation

$$\partial_t(d/2) = R_{\text{diss}}\,\chi_A\nu_A - R_{\text{prec}}\,\chi_E\nu_E = k_1^{\text{eff}}\chi_A\nu_A c_B - k_2^{\text{eff}}\chi_E\nu_E c_C, \tag{12}$$

with the first term accounting for dissolution of A and the second—precipitation of E. In the above, ν_A and ν_E are the molar volumes of the dissolved and precipitated rock material A and E respectively. Integrating the above along the pore, we can calculate the total change in the mineral volume per unit time due to dissolution and precipitation in a single pore:

$$\Delta V = \Delta V^A + \Delta V^E = \pi d\Delta t\int_0^l \left(-k_1^{\text{eff}}\chi_A\nu_A c_B(x) + k_2^{\text{eff}}\chi_E\nu_E c_C(x)\right)dx, \tag{13}$$

with the volume change of mineral A, ΔV^A, and that of mineral E, ΔV^E, given by

$$\begin{aligned}\Delta V^A &= -q\Delta t\chi_A\nu_A c_{B0}\left(1-e^{-\text{Da}_1}\right),\\ \Delta V^E &= q\Delta t\chi_E\nu_E\left(c_{C0}\left(1-e^{-\text{Da}_2}\right) - c_{B0}\frac{\text{Da}_1\left(1-e^{-\text{Da}_2}\right) - \text{Da}_2\left(1-e^{-\text{Da}_1}\right)}{\text{Da}_1-\text{Da}_2}\right).\end{aligned} \tag{14}$$

As previously mentioned, one of the underlying assumptions in pore-network models for chemically transforming porous media (Budek & Szymczak, 2012; Hoefner & Fogler, 1988) is that the pores widen uniformly while maintaining their cylindrical shape. Consequently, the change in channel volume by ΔV corresponds to a change in diameter during a time step Δt:

$$\begin{aligned}\frac{\Delta d}{d^0} = -\frac{2\Delta V}{\pi l d d^0} = \frac{\Delta t'}{\text{Da}_1(1+\frac{k_1 d}{D\text{Sh}})c_B^{in}}\Bigg(&c_{B0}\left(1-e^{-\text{Da}_1}\right)\\ &- c_{C0}\Gamma\left(1-e^{-\text{Da}_2}\right) - c_{B0}\Gamma\frac{\text{Da}_1\left(1-e^{-\text{Da}_2}\right) - \text{Da}_2\left(1-e^{-\text{Da}_1}\right)}{\text{Da}_1-\text{Da}_2}\Bigg),\end{aligned} \tag{15}$$

where the dimensionless time was introduced as

$$\Delta t' = \frac{2k_1\chi_A\nu_A c_B^{\text{in}}}{d^0}\Delta t. \tag{16}$$

Here, d^0 represents the characteristic diameter of a pore, typically taken as the average diameter at the initial state of the system and c_B^{in} is the concentration of species B at the inlet of the system. Additionally, we have introduced the ratio of molar volume of precipitating rock to dissolving one:

$$\Gamma = \frac{\chi_E\nu_E}{\chi_A\nu_A}. \tag{17}$$

This ratio plays a crucial role in the geometry evolution; $\Gamma < 1$ corresponds to the reaction accompanied by porosity creation, whereas $\Gamma > 1$ leads to reactions coupled with an increase in solid volume, potentially resulting in self-clogging. However, as this work will demonstrate, dissolution-precipitation patterns depend not only on Γ but also on the kinetics of the reactions.

Faithful representation of dissolution-precipitation processes requires not only tracking of the evolving diameters of the pores, but also of the total volume of A and E minerals in the grains in between the pores. The system considered in this work is assumed to be quasi-2D with a fixed thickness in the vertical direction (z) much smaller than the size of the system along x and y. Such a system can, for example, be a model of a bedding plane where the average pore size is comparable to the grain size of the confining rock (Dreybrodt, 1988; Ewers, 1982), or it can be

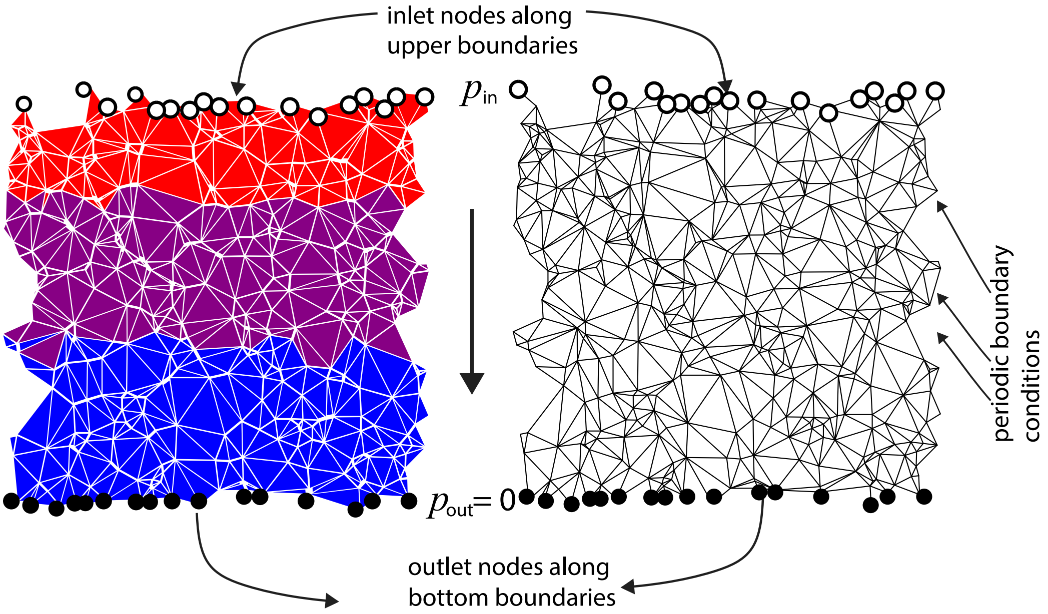

Figure 3. Pores and grains: The model consists of a random assembly of triangular grains surrounded by pores. The size of each grain changes in response to reactions occurring in the surrounding pores. During each time step, both pore diameters and pore lengths are updated, and grain volumes are recalculated. The grains are comprised of either mineral A (depicted in blue), mineral E (depicted in red), or a mixture of the two (various shades of purple).

representative of quasi-2D experimental systems (Cochepin et al., 2008; Poonoosamy et al., 2015; Trotignon et al., 2005) designed to study flow-induced chemical transformations in porous media.

In our network model, triangular grains of rock material are located in between the pores (see Figure 3), consisting of a primary (dissolving) mineral *A* (which we mark in blue) and a secondary (precipitating) mineral *E* (red). The initial diameters of all the pores are set to d^0, and all the grains consist initially of mineral *A* only. The initial volumes of the grains are determined based on the distances between nodes and reduced by the volume occupied by the pores. Based on this, the initial lengths of the channels are also determined. As the hydrochemical transformation of the porous medium proceeds, the volumes of the grains change. In our model, we then rescale the grains to either larger or smaller size, as illustrated in Figure 4.

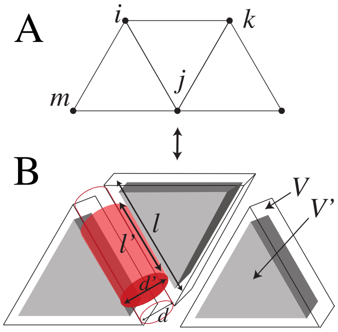

Figure 4. Schematic of pore growth and associated grain shrinkage. The network, consisting of nodes and edges, is shown in the upper panel, while the evolution of volume and shape for both pores and grains is illustrated in the lower panel. An edge *ij* corresponds to a pore shaded in red, with two adjacent grains, *mij* and *ijk*, shaded in gray. The original size of the grain is outlined with black lines, while the solid gray area represents the grain after dissolution. Due to the pore widening, the lengths of the pores are decreasing. The grain shapes are assumed to scale uniformly during dissolution.

Based on Equations 13–15, we can calculate new pore diameters, d', and new grain volumes, V'. We assume that the volume increments ΔV_{ij}^A and ΔV_{ij}^E calculated based on Equation 14 are equally distributed among all the grains (*ijk*) adjacent to a given pore (*ij*). This allows us to determine the updated diameters and lengths of individual pores, as well as the new volumes of the grains:

$$d'_{ij} = d_{ij} - \frac{2\left(\Delta V_{ij}^A + \Delta V_{ij}^E\right)}{\pi l_{ij} d_{ij}}, \tag{18}$$

$$V'_{ijk} = V_{ijk} + \frac{1}{2}\left(\Delta V_{ij}^A + \Delta V_{ij}^E + \Delta V_{jk}^A + \Delta V_{jk}^E + \Delta V_{ki}^A + \Delta V_{ki}^E\right), \tag{19}$$

$$l'_{ij} = \frac{1}{2}\left(\left(\frac{V'_{\text{ijk}}}{V^0_{\text{ijk}}}\right)^{1/3} + \left(\frac{V'_{\text{ijm}}}{V^0_{\text{ijm}}}\right)^{1/3}\right) l^0_{ij}, \tag{20}$$

where ΔV_{ij}^A and ΔV_{ij}^E are the mineral volume increments in pore *ij*. To calculate the new pore lengths, we first assume the uniform scaling of grain shapes and then calculate the final l'_{ij} as the average over all surrounding grain

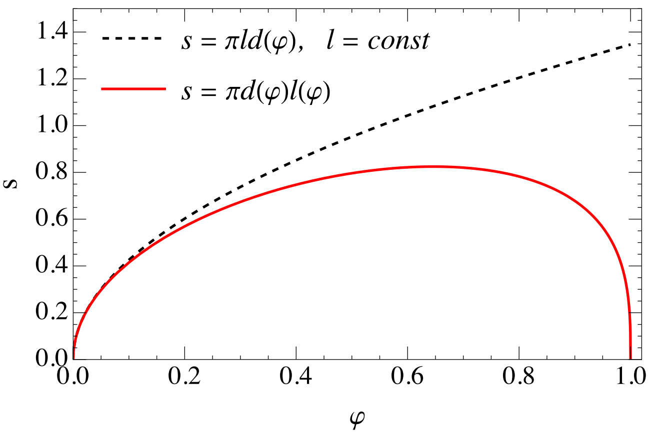

Figure 5. Porosity versus reaction surface in a uniform system with triangular grains and cylindrical pores (red line) compared to similar relation with system in which pore length is constant (black dashed line).

lengths. The maximal length of a pore, l_{ij}^0, is given by the distance between spanning nodes (i,j). The average distance between connected nodes (over all pores in the network), $l^0 = \langle l_{ij}^0 \rangle$, will be used as a unit of length in the system. Additionally, we assume that the system has a certain thickness in the third (vertical) dimension, which we take to be equal to $l^0/2$. Thus, the maximal volume of a grain spanned between nodes (i,j,k) will be given by $V_{ijk}^0 = S_{\triangle_{ijk}} l^0/2$.

Note that, unlike in Budek and Szymczak (2012), in this model, the reaction surface of a pore, represented by $s(d) = \pi d l(d)$, is not a monotonic function of its diameter or porosity, $\varphi = \frac{V^0 - V}{V^0}$. For symmetrical, hexagonal network of pores the relation between the reaction surface and porosity is as follows:

$$s(\varphi) = \frac{3^{3/4}\pi^{1/2}}{2}\left(1 - (1-\varphi)^{2/3}\right)^{1/2}(1-\varphi)^{1/3}, \tag{21}$$

and attains its maximum at $\varphi = 1 - \frac{\sqrt{2}}{4}$ (as shown in Figure 5). As porosity increases, the reaction surface rapidly expands (mainly driven by changes in diameter, d), reaching a plateau at approximately $\varphi \simeq 0.4$. Beyond $\varphi > 0.8$, it sharply decreases to zero primarily due to a decrease in l. This behavior mirrors realistic characteristics of the reactive surface area, akin to what is observed in experiments and theoretically described, for instance, in terms of the sugar-lump model presented in Noiriel et al. (2009). In this model, the porous medium is assumed to comprise a cluster of grains that progressively dissociate as each grain undergoes dissolution, resembling the process of sugar dissolving in a cup of coffee. The sugar-lump model offered the most accurate fit for the data on reactive surface area obtained from laboratory flow-through experiments.

A finite amount of mineral A and a finite amount of space for precipitation impose additional constraints on our system. In channels that lack access to grains containing A, the dissolution reaction stops. If precipitation dominates over dissolution, the significant decrease in pore diameters may cause numerical problems when calculating the flow field through the system. Permeability depends on the channel diameter to the fourth power (see Equation 1), making the solution of the continuity equations for flow numerically unstable if diameters (d) differ by many orders of magnitude between different pores. To circumvent this technical issue, we remove all pores with $d < d_{\min} = 0.0001 l^0$. Note that this approach may eventually result in a lack of connection between inlet and outlet nodes. In such a case, we terminate the simulation and interpret it as a total clogging of the system.

Due to the linear nature of governing equations, for a given initial geometry of the system and value of d^0, the parameters that determine the emerging patterns are Γ and the initial mean values of the effective Damköhler number

$$\mathrm{Da}_i^0 = \frac{\pi d^0 l^0 k_i^{\mathrm{eff}}(d^0)}{q^0}, \tag{22}$$

where d^0, l^0, and q^0 denote the initial average values of diameters, lengths, and flows in all the channels, respectively.

Instead of characterizing the results in terms of two Damköhler numbers, Da_1^0 and Da_2^0, we will find it more convenient to introduce the ratio of dissolution and precipitation rate constant

$$\kappa = \frac{k_2^{\mathrm{eff}}(d^0)}{k_1^{\mathrm{eff}}(d^0)}, \tag{23}$$

which unequivocally determines the ratio $\mathrm{Da}_1^0/\mathrm{Da}_2^0$. Thus, by changing Da_1^0 and κ, we cover the same parameter space as by varying Da_1^0 and Da_2^0. Later, for simplicity, we will omit the indices and write $\mathrm{Da} \equiv \mathrm{Da}_1^0$.

To a lesser extent, the dissolution patterns will also depend on the transport parameter

$$G_i = \frac{k_i d^0}{D_i \mathrm{Sh}}, \tag{24}$$

characterizing the hindering effect of transverse diffusion across the pore on the reaction rate. The impact of G on the dissolution patterns is known to be much weaker than that of Da (Budek & Szymczak, 2012), mostly affecting the aspect ratio of the emerging dissolution channels. In this work, to limit the number of free parameters in the system, we perform the simulations with a fixed value of G_i parameters, $\mathrm{G}_i = 1$, which implies a mixed transport/reaction control on the reaction rate, characteristic of acidization experiments. For example, dissolution of Indiana limestone by hydrochloric acid with surface reaction rate $k = 0.2$ cm/s results in $\mathrm{G} \approx 0.7$.

The pore-network models of porous media that track both dissolution and precipitation reactions were first developed by Rege and Fogler (1989), building upon the earlier dissolution-only models by Hoefner and Fogler (1988). Inspired by these works, our model expands it in several ways. The most important new element is the tracking of not only pores but also solid material grains and their composition. This allows us to monitor the concentrations of reactants and products more effectively and to model the evolution of the reaction surface area in a more realistic manner. Both pore diameter and length now change during the simulation. Additionally, this approach enables us to determine if the soluble material is still present in a grain before performing dissolution. On a technical level, we utilize a fast, parallel sparse matrix solver, which we find more efficient compared to the stochastic concentration tracking method used in Rege and Fogler (1989).

4. One-Dimensional Solutions

Before delving into the analysis of two-dimensional dissolution-precipitation patterns, it is worthwhile to examine the behavior of the system in one dimension. In this scenario, we assume that the concentrations of reactants and products, along with pore diameters, are only functions of the distance from the system inlet. Figure 6 shows the emerging profiles of c_B, c_C, the total porosity of the system φ, as well as v_A and v_E–the volume fractions of minerals A and E. The simulation was executed on a regular hexagonal network comprising $4 \times 2{,}000$ nodes, with periodic boundary conditions on the lateral sides of the system.

Figure 6a illustrates the results for $\mathrm{Da} = 0.02$, $\kappa = 1.0$, $\Gamma = 1.0$, and $d^0 = 0.3$. Initially, the system was filled with the primary mineral A, with an initial volume fraction $v_A\left(d^0 = 0.3\right) \approx 0.69$, corresponding to an initial porosity of $\varphi_0 = 0.31$. This system was then infiltrated with a fluid containing B. All concentrations are scaled by the inlet concentration of B, c_B^{in}. At the reaction front, the concentration of c_B decays exponentially due to the dissolution reaction. The penetration length of B is given by $L_B = l^0/\mathrm{Da}$. As a result of dissolution, C ions are produced, whose concentration initially increases but then decreases due to precipitation. The penetration length of C, L_C, depends on κ: $L_C \sim L_B/\kappa$.

It is important to note that porosity decreases at the front. This is the consequence of precipitation occurring further in the system than dissolution; thus, at the front mineral E has already been deposited, but A has not yet fully dissolved. Since the molar volume ratio is set to one, $\Gamma = 1$, the final porosity of the system equals the initial one for the simulation depicted in Figure 6a.

Results of the simulation for different parameters, $\Gamma = 1.2$ and $\kappa = 5$, are presented in Figure 6b. Note that even though the volume ratio, Γ, is now larger than one, the system does not get clogged. As long as there is enough void space in the system, a stationary solution exists with the front moving downstream, similarly to the previous case. The condition for such a solution to exist is that the minimal porosity, attained by the system at the reaction front, be larger than zero.

The parameter Γ, which determines the total volume gain or loss in the reaction, controls the final porosity of the system. Behind the front, the primary species (A) is completely replaced by the secondary species (E) with the volume fraction v_E^{final}, which—due to mass conservation—is equal to Γv_A^0 (in the case of Figure 6b, $v_E^{\mathrm{final}} = 0.83$). The value of the final porosity is then $\varphi_{\mathrm{final}} = 1 - \Gamma\left(1 - \varphi_0\right)$.

The role of the Damköhler number, Da, in a one-dimensional system can be reduced to the change of length scale. Indeed, by scaling $x' = \mathrm{Da}\, x$, we can map systems with different Da onto each other (see Equation 10). On the

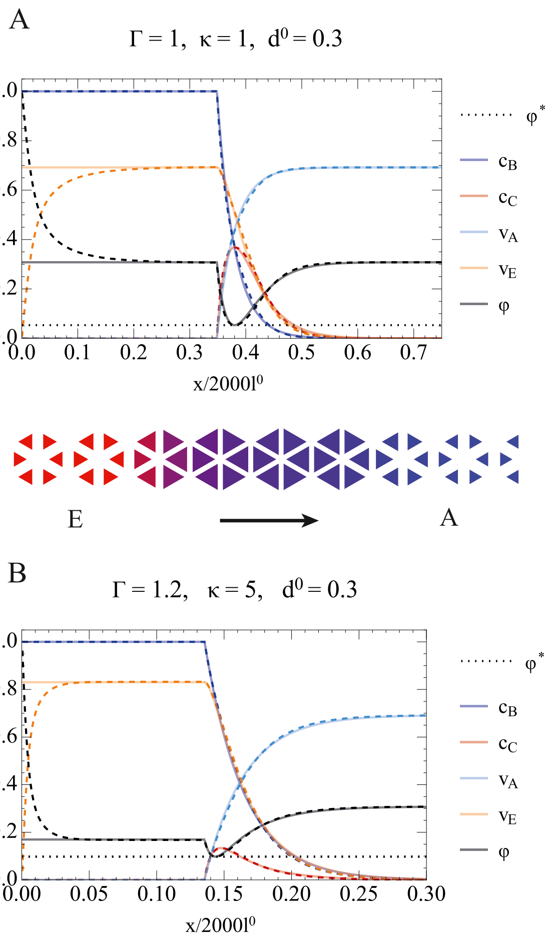

Figure 6. A one-dimensional solution for a system with dissolution and precipitation for different Γ and κ values. Numerical simulation results are shown as dashed lines, while solid lines represent the analytical solution of Equation A1 given by Equation A2. The minimal porosity (see Equation A4) is indicated by a black dotted line. Note that all concentrations are scaled by c_B^{in}. Panel (a) corresponds to $\Gamma = 1$ (A and E species have the same molar volume) and $\kappa = 1$ (dissolution and precipitation reaction rates are equal). In this case, the initial and final porosities are identical. Panel (b) corresponds to $\Gamma = 1.2$ and $\kappa = 5$ where the final porosity is smaller than the initial one. In both cases, the porosity reaches a minimum at the front, which is deeper for lower values of κ.

other hand, the parameter κ influences the shapes of both $c_C(x)$ and $v_E(x)$, decreasing the penetration length of C ions as κ increases. Finally, the initial pore diameter, d^0, primarily impacts the front profile by altering the initial and final porosity and the resultant volume of the secondary mineral, v_E.

To determine the condition for clogging in terms of κ, Γ, in Appendix A we consider an effective, Darcy-scale description of our system. Under these conditions, the concentration and mineral volume profiles can be explicitly determined, provided that we assume a constant reactive surface area, $s(\varphi) = const$. The detailed solution is presented in Appendix A. Furthermore, a comparison between the analytical solution and our numerical model is illustrated in Figure 6. The agreement between them is nearly perfect, provided that we operate in a regime where the surface area does not undergo significant changes (see Figure 5).

Using the analytical solution for porosity, we can identify the conditions under which it remains positive (i.e., no clogging occurs). This leads to the following condition for the initial porosity φ_0 in terms of Γ and κ

$$\Gamma\left(\frac{(\Gamma-1)\kappa+1}{\Gamma\kappa}\right)^{\frac{\kappa}{\kappa-1}} < \frac{\varphi_0}{1-\varphi_0}. \tag{25}$$

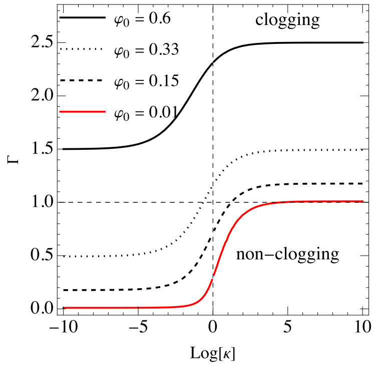

Figure 7. The threshold volume ratio value, Γ^* (Equation 25) above which the medium gets clogged for a 1D system as a function of κ for four different values of the initial porosity, φ_0.

This condition ensures that the system remains permeable by preventing the porosity from dropping to levels that could cause clogging.

The contour lines representing the above condition for different initial porosities, φ_0, are shown in Figure 7. The higher the initial porosity, the broader the parameter space (κ, Γ) that avoids clogging. A slow precipitation rate, characterized by a small κ, facilitates clogging. To elucidate this, consider a point the distance of which from the dissolution front, L, is larger than the dissolution penetration length $(L > L_B)$ yet smaller than the precipitation penetration length $(L \ll L_C)$. Such a condition can be easily fulfilled, since $L_B/L_C = \kappa \ll 1$. At such a point, mineral A is still intact, thus the volume fraction left for E to precipitate is equal to the initial porosity, φ_0. Clogging will thus occur if $v_E^{\text{final}} \geq \varphi_0$. Since $v_E^{\text{final}} = \Gamma v_A^0 = \Gamma(1 - \varphi_0)$, we finally obtain the following limit for maximal non-clogging volume ratio, $\Gamma^*_{\kappa\to 0} = \frac{\varphi_0}{1-\varphi_0}$.

Conversely, for rapid precipitation reactions, this threshold value, Γ^*, increases. In the case of large κ, precipitation occurs in situ, with the dissolution of mineral A followed immediately by the precipitation of E at the same place. In such a case, E can fill the entire volume, that is, $v_E^{\text{final}} = \Gamma v_A^0 \leq 1$. Thus, the maximal non-clogging Γ is then $\Gamma^*_{\kappa\to\infty} = \frac{1}{1-\varphi_0}$.

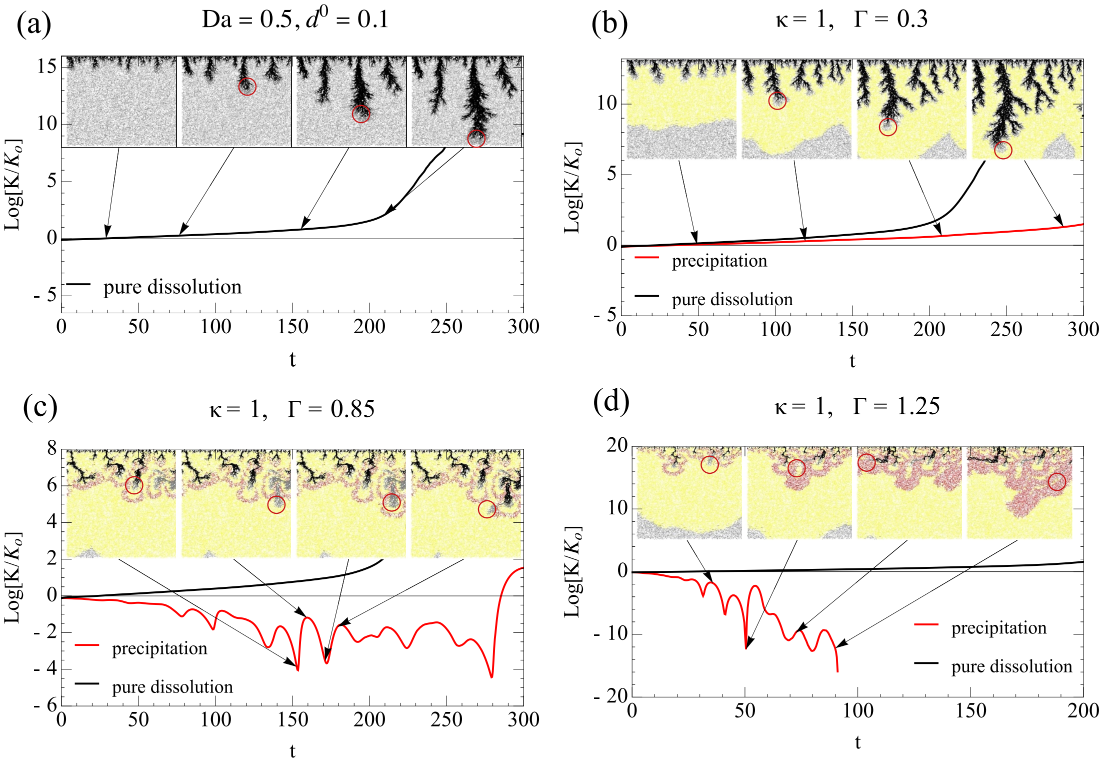

Figure 8. The evolution of dissolution patterns for different Γ values, with fixed Da $= 0.5$, $d^0 = 0.1$, and $\kappa = 1$, alongside the respective permeability evolution curves. Active channels are marked by red circles. Pores are color-coded as follows: heavily overgrown pores $(d \leq d^0/10)$ are red; intermediate pores $(d^0/10 < d \leq d^0)$ are yellow; pores larger than d^0 but smaller than $2d^0$ $(d^0 < d < 2d^0)$ are gray; and pores forming the dissolution pattern $(d \geq 2d^0)$ are black. In panel (a), the simulation for $\Gamma = 0$ represents pure dissolution. Panel (b) corresponds to $\Gamma = 0.3$, where weak precipitation slows down the breakthrough. In panel (c), the simulation results for $\Gamma = 0.85$ are presented, showing strong competition between dissolution and precipitation, accompanied by characteristic oscillations in permeability. In panel (d), with $\Gamma = 1.25$, precipitation is stronger than dissolution, leading to clogging. Movies S2, S3, S4, S5 illustrate evolution of the patterns in time.

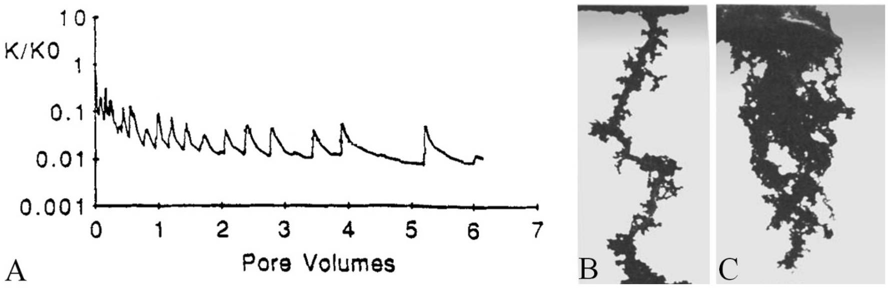

Figure 9. (a) Permeability evolution in the experiments of Rege and Folger (Rege & Fogler, 1989) with dissolution of calcite and precipitation of ferric hydroxide in limestone cores (Rege & Fogler, 1989) (b, c) Wood's metal castings of the dissolution patterns in Rege & Fogler experiments: pure dissolution (b) and the interplay of dissolution and precipitation (c).

5. Permeability Oscillations and Clogging

Let us now shift our focus to the two-dimensional case to explore how the development of dissolution patterns in the system and the evolution of its total permeability, K, are influenced by the precipitation reaction. Our reference scenario uses $\mathrm{Da} = 0.5$ and $d^0 = 0.1$. The process of pure dissolution with these parameters (with precipitation reaction switched off) on a random grid of 100×100 pores is shown in Figure 8a. The initial network is generated from nodes uniformly distributed on a square, with pores defined by the edges of the Delaunay triangulation. All pores have the same initial diameters, and the only source of randomness is the placement of network nodes, which influences initial pore lengths and grain volumes. In this reaction regime, relatively narrow (a few pores wide) and highly branched dissolution channels form. Initially, multiple channels begin to grow, but intense competition for flow and reactant leads to a gradual reduction in the number of active channels. Eventually, only one channel manages to reach the end of the system. Initially, the total permeability of the system increases slowly as the dissolution channels develop. Then, it begins to rise much more rapidly once the main channel breaks through to the end of the system.

Figure 8b presents results for the same system, but this time with precipitation characterized by $\kappa = 1$ and $\Gamma = 0.3$, indicating a relatively small molar volume of the secondary mineral (E). The pattern displays dissolution channels that are similar to those in the previous case, yet slightly thicker and more branched. Upon closer inspection, one can observe that the competition between channels is less intense: at any given moment, there are more active channels than in the scenario without precipitation. This is attributed to the fact that the partially cemented rock, which is of low porosity and rich in the secondary mineral, forms protective barriers around the dissolution channels, hindering interactions between them. Notably, the permeability increases more slowly than in the pure dissolution scenario, and the breakthrough occurs later.

Let us now consider the scenario where the molar volumes of minerals A and E are of similar order, $\kappa = 1$ and $\Gamma = 0.85$ (Figure 8c). In the figure, areas with lower than initial porosity are marked in yellow, while intensely overgrown areas are marked in red $\left(d \leq d^0/10\right)$. In this case, one can observe intense competition between dissolution and precipitation, resulting in intriguing, tortuous dissolution patterns. The emerging wormholes, where dissolution initially concentrates, are also the regions of most intense precipitation. This leads to the clogging of the flow path around an active dissolution channel and the subsequent formation of a new one attempting to bypass the clogged regions. Sometimes, these channels grow in directions transverse to the main pressure gradient or even backtrack. However, after some time, the growth of a new channel is again halted by a decrease in porosity in front of its tip, prompting another channel to begin growing, only to eventually become overgrown as well. Consequently, the permeability evolution over time experiences continuous oscillations, with each maximum in permeability corresponding to an attempt by one of the most active fingers to break through (active fingers are highlighted by red circles in Figure 8). Ultimately, one of the channels manages to break through to the end of the system, although it is challenging to predict which one will succeed. Unlike in pure dissolution scenarios, where the longest channel almost always prevails, the outcome here remains uncertain until the very end, with no clear indication of which channel will dominate and reach the system's end. The resulting dissolution patterns can significantly deviate in morphology from those observed in pure dissolution cases. Interestingly, similar oscillations in permeability have been experimentally observed by

Rege and Fogler (1989). In their experiments, limestone cores were infiltrated by a mixture of HCl and $FeCl_3$, resulting in the dissolution of calcite and precipitation of ferric hydroxide (see Figure 9). They observed pronounced oscillations in permeability, which they attributed to the formation of cemented regions in the medium. The frequency of these oscillations decreased with an increasing flow rate, since a larger flow tends to spread the precipitate more evenly in the system, which slows down the clogging. Rege and Folger succeeded in casting dissolution patterns of their samples by injecting Wood's metal in the pore space. Their results show that the interplay of dissolution and precipitation results in much more ramified patterns which involve a considerable larger portion of pore space than the pure dissolution patterns obtained at the same flow rate. We will return to this point in Section 6.

Permeability oscillations were also observed in the studies of Singurindy and Berkowitz (2003b) who flooded calcareous sandstone by a mixture of HCl/H_2SO_4 triggering calcite dissolution and gypsum precipitation. Post-mortem analysis of the samples revealed that gypsum precipitated around the wormholes effectively cementing it, not unlike the patterns observed in Figure 8c.

Finally, let us consider the case of even more intense precipitation ($\Gamma = 1.25$ and $\kappa = 1$). As before, the permeability oscillates over time, and channels intensely meander in search of an exit route (see Figure 8d). However, the system eventually becomes completely clogged. Since in the code we remove all channels with $d \leq d_{\min}$, at some point, the last connection between inlet and outlet is cut off, and the simulation stops.

Let us now systematically analyze the clogging of the system to identify the specific parameters $\mathrm{Da}, \Gamma, \kappa, d^0$ that lead to complete cementation. This time, the simulations are conducted on a grid spanning 50×200 randomly selected points. The simulation terminates either upon the breakthrough of a dissolution/precipitation channel or when the connection between the inlet and outlet nodes is broken due to clogging. For each set of parameters, the simulation is repeated 40 times with different random network node placements and the results are averaged over these realizations.

For the purpose of data analysis, we define a dissolution channel as a set of interconnected pores, starting from the inlet, whose diameters exceed $2d^0$. This definition is intuitive in the dissolution-dominated regime. However, under conditions of large Γ or high initial porosity, the areas of intense dissolution and precipitation may not necessarily exhibit higher porosity than the initial state due to the substantial amount of precipitated secondary mineral E. In such cases, we alternatively define a precipitation channel as being composed of grains where $v_E > v_A/2$, and in contact with the inlet. We terminate the simulation when either the dissolution or precipitation channel reaches the outlet. The breakthrough of a dissolution channel to the outlet of the system is always associated with a significant increase in system permeability, a phenomenon not consistently observed with precipitation channels, especially when $\Gamma \geq 1$. Nonetheless, since dissolution and precipitation reactions primarily concentrate around the tip of the active dissolution/precipitation channel, reaching the outlet is considered a natural point to conclude the simulation.

The clogging behavior in a finite system also depends on its total length, L, due to potential leakage of reagents from the system. Therefore, for a finite L, the ratio of the dissolution/precipitation penetration lengths to the system size becomes important:

$$\tilde{L}_B := \frac{L_B}{L} = \frac{l^0}{L}\frac{1}{\mathrm{Da}} \quad \text{and} \quad \tilde{L}_C := \frac{L_C}{L} = \frac{l^0}{L}\frac{1}{\kappa \mathrm{Da}}. \tag{26}$$

If $\tilde{L}_B, \tilde{L}_C \ll 1$, the leakage of reagents may be neglected. However, for $\tilde{L}_B, \tilde{L}_C \sim 1$, the leakage of the coupling ion becomes significant, reducing the likelihood of clogging.

Figure 10 presents the fraction of simulation runs resulting in dissolution/precipitation channel breakthrough for different parameter values $\{\mathrm{Da}, \Gamma, \kappa, d^0\}$. Additionally the information about $\tilde{L}_C$ is provided. The upper left panel shows results for low initial porosity $(d^0 = 0.1, \varphi_0 = 0.04)$, and $\mathrm{Da} = 0.5$. In one-dimensional model, such porosity values correspond to critical $\Gamma^*_{\kappa\to 0} = 0.04$ and $\Gamma^*_{\kappa\to\infty} = 1.04$. For $\Gamma > \Gamma^*$ we should get clogging, while smaller Γ values should lead to the breakthrough. Analyzing the clogging probability in 2D, we recognize the sigmoidal boundary between clogging and breakthrough regimes predicted by the one-dimensional model (see Figure 7). This is particularly evident for large κ (small $\tilde{L}_C$), indicating the critical value of $\Gamma^*_{\kappa\to\infty}$ to be around 1.

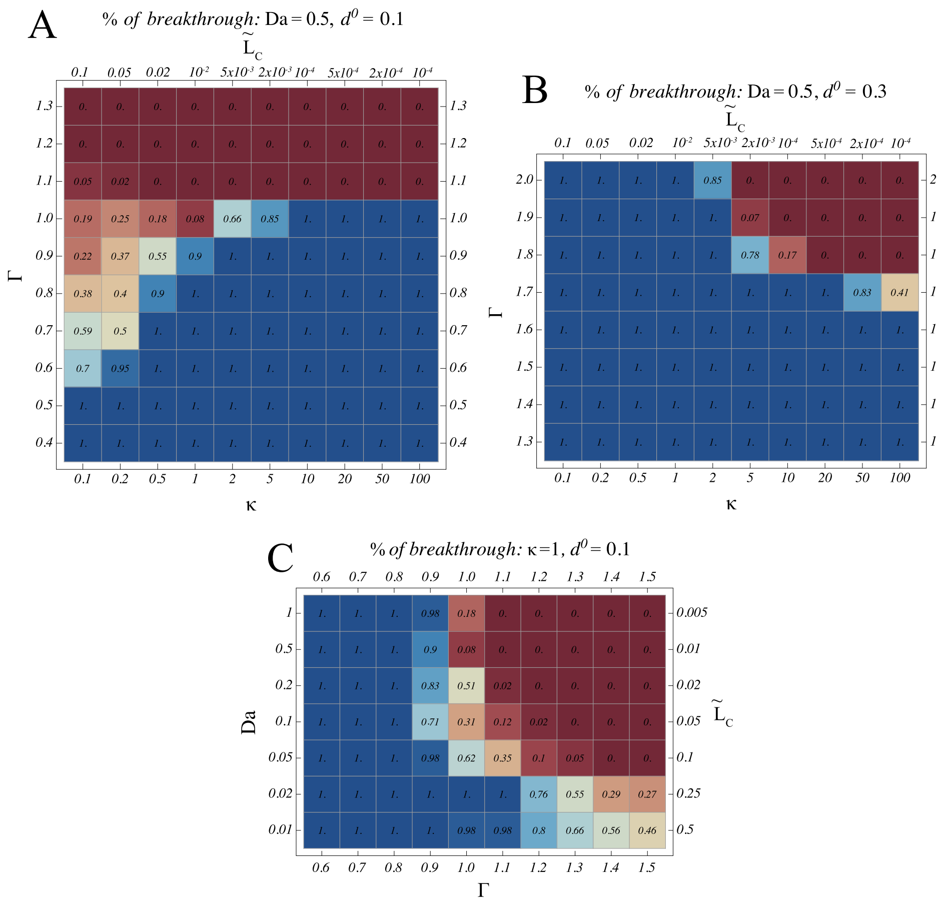

Γ	0.1	0.2	0.5	1	2	5	10	20	50	100
1.3	0.	0.	0.	0.	0.	0.	0.	0.	0.	0.
1.2	0.	0.	0.	0.	0.	0.	0.	0.	0.	0.
1.1	0.05	0.02	0.	0.	0.	0.	0.	0.	0.	0.
1.0	0.19	0.25	0.18	0.08	0.66	0.85	1.	1.	1.	1.
0.9	0.22	0.37	0.55	0.9	1.	1.	1.	1.	1.	1.
0.8	0.38	0.4	0.9	1.	1.	1.	1.	1.	1.	1.
0.7	0.59	0.5	1.	1.	1.	1.	1.	1.	1.	1.
0.6	0.7	0.95	1.	1.	1.	1.	1.	1.	1.	1.
0.5	1.	1.	1.	1.	1.	1.	1.	1.	1.	1.
0.4	1.	1.	1.	1.	1.	1.	1.	1.	1.	1.

Γ	0.1	0.2	0.5	1	2	5	10	20	50	100
2.0	1.	1.	1.	1.	0.85	0.	0.	0.	0.	0.
1.9	1.	1.	1.	1.	1.	0.07	0.	0.	0.	0.
1.8	1.	1.	1.	1.	1.	0.78	0.17	0.	0.	0.
1.7	1.	1.	1.	1.	1.	1.	1.	1.	0.83	0.41
1.6	1.	1.	1.	1.	1.	1.	1.	1.	1.	1.
1.5	1.	1.	1.	1.	1.	1.	1.	1.	1.	1.
1.4	1.	1.	1.	1.	1.	1.	1.	1.	1.	1.
1.3	1.	1.	1.	1.	1.	1.	1.	1.	1.	1.

Da	0.6	0.7	0.8	0.9	1.0	1.1	1.2	1.3	1.4	1.5
1	1.	1.	1.	0.98	0.18	0.	0.	0.	0.	0.
0.5	1.	1.	1.	0.9	0.08	0.	0.	0.	0.	0.
0.2	1.	1.	1.	0.83	0.51	0.02	0.	0.	0.	0.
0.1	1.	1.	1.	0.71	0.31	0.12	0.02	0.	0.	0.
0.05	1.	1.	1.	0.98	0.62	0.35	0.1	0.05	0.	0.
0.02	1.	1.	1.	1.	1.	1.	0.76	0.55	0.29	0.27
0.01	1.	1.	1.	1.	0.98	0.98	0.8	0.66	0.56	0.46

Figure 10. (a) Fraction of simulation runs resulting in breakthrough for Da $= 0.1$, $d^0 = 0.1$, and varying Γ and κ. Red indicates clogging, while blue represents breakthrough. A sigmoidal boundary separates parameter sets leading to breakthrough and clogging (see Equation 7). (b) Fraction of simulation runs for Da $= 0.1$ and $d^0 = 0.3$, showing no sigmoidal boundary due to higher initial permeability. (c) Probability of clogging as a function of Da and Γ, with fixed $\kappa = 1$ and $d^0 = 0.1$.

For smaller κ $\left(\tilde{L}_C > 0.01\right)$, the sigmoidal boundary becomes blurred, with some simulations resulting in clogging while others do not.

The lower bound of the 1D model, $\Gamma^*_{\kappa\to 0} = 0.04$, does not seem to correlate with the 2D network simulations. For $\kappa = 1$, the one-dimensional case predicts a critical Γ of 0.42, whereas in 2D, the corresponding transition occurs around $\Gamma \approx 0.8$. These discrepancies are caused by the fact that the 1D theory was derived for an infinite system, whereas for 2D simulations with small κ, the finite size of the system starts to matter—a significant amount of C ions leave the system before they can precipitate as E. On the other hand, in the 2D system, non-uniform dissolution front and reaction channeling provide more opportunities to avoid complete clogging. Thus, the one-dimensional model establishes a lower bound for Γ^*, with actual values in 2D often being higher.

The fraction of breakthrough for a system with a higher initial porosity $\left(d^0 = 0.3, \varphi_0 = 0.33\right)$ is shown in Figure 10b. This initial pore diameter corresponds to 1D critical values $\Gamma^*_{\kappa\to 0} = 0.48$ and $\Gamma^*_{\kappa\to\infty} = 1.48$. For large κ (small $\tilde{L}_C$), once again, the agreement with the predictions of the one-dimensional model is rather good. In this regime, dissolution is almost immediately followed by precipitation so that C ions produced in a given pore precipitate in the same pore. Additionally, it should be noted that for $\kappa \to \infty$, the critical Γ^* must satisfy $\Gamma^*_{\kappa\to\infty} = \frac{1}{1-\varphi_0} > 1$, resulting in a final porosity lower than the initial. Consequently, there is no mechanism causing an instability of the reaction front, resulting in a flat front where substance A is replaced by E in both one and two dimensions.

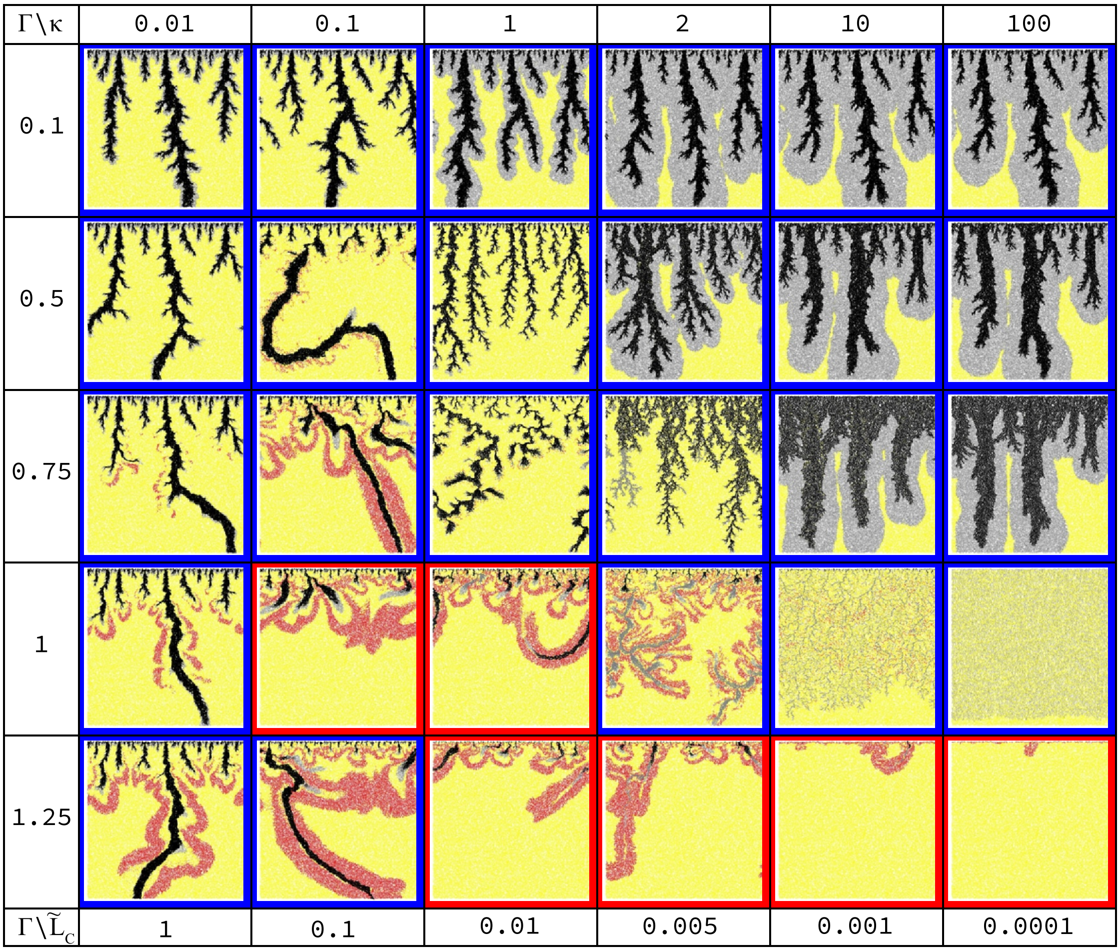

Figure 11. Morphological phase diagram of dissolution-precipitation patterns for various Γ and κ values, with Da = 0.5 and $d^0 = 0.1$ (pore diameter maps). Pores are color-coded as follows: heavily overgrown pores $\left(d \le d^0/10\right)$ are red; intermediate pores $\left(d^0/10 < d \le d^0\right)$ are yellow; pores larger than d^0 but smaller than $2d^0$ $\left(d^0 < d < 2d^0\right)$ are gray; and pores forming the dissolution pattern $\left(d \ge 2d^0\right)$ are black. The lower axis shows corresponding values of the precipitation penetration length, $\tilde{L}_C$.

For such a high value of initial porosity, the sigmoid characterizing 1D clogging condition is entirely absent: smaller κ leads to a higher breakthrough probability for a given Γ, which is the opposite trend to that predicted by a 1D model. There are two reasons for this. First, large initial diameters imply that cementation processes take considerable time. Second, the highly effective dissolution channeling observed at high porosities leads to increased flow rates and intense leaching of the C ions due to the locally decreased Damköhler number, resulting in an increase in both $\tilde{L}_B$ and $\tilde{L}_C$.

The value of the Damköhler number itself does not influence clogging in an infinite one-dimensional system (see Appendix A). However, this behavior differs in a 2D system of finite length. The lower panel of Figure 10 shows the breakthrough probability as a function of Da and Γ for fixed $d^0 = 0.1$ and $\kappa = 1$. Small Da values lead to an increase of breakthrough probability by enhancing leaching (larger $\tilde{L}_C$) and making it easier for dissolution channels to bypass clogged areas, as the channels are wider at smaller Da. Summarizing, the 1D estimation for clogging/breakthrough provides a lower bound for $\Gamma^*\left(\kappa, d^0\right)$. In 2D finite systems, Γ^* can be higher, particularly for small κ (resulting in large $\tilde{L}_C$) and large initial porosity.

6. Morphological Diagrams

Let us examine the morphology of dissolution-precipitation patterns for different values of κ and Γ. Our reference case will again be Da = 0.5 and $d^0 = 0.1$. Simulations are conducted on a grid consisting of 200 × 200

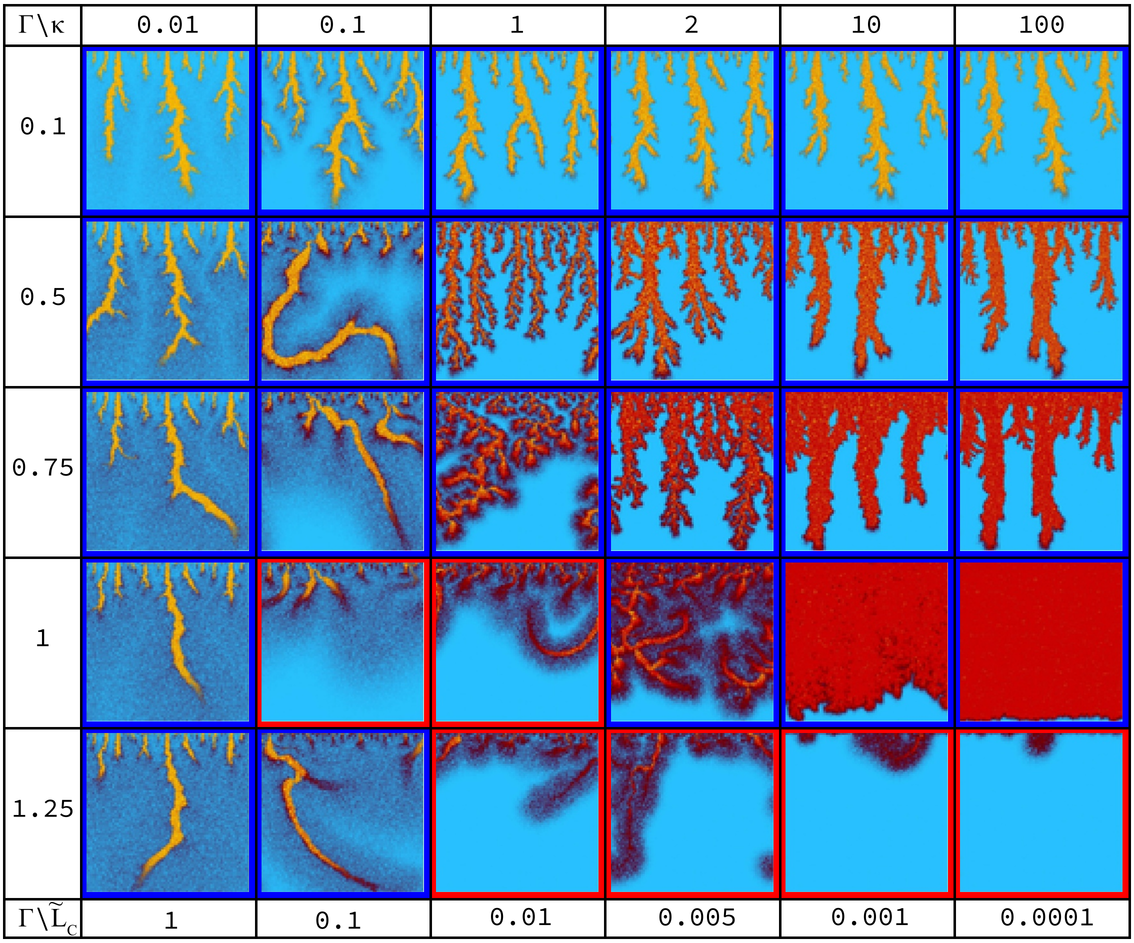

Figure 12. Morphological phase diagram of dissolution-precipitation patterns for different Γ and κ for Da = 0.5, $d^0 = 0.1$ (mineral maps). Colors correspond to the mineral concentrations in the grains: mineral A is marked in blue, mineral E—red while the mixtures of the minerals are marked by various shades of purple. Note that an empty space, not occupied by grains, is marked in yellow. The lower axis shows corresponding values of the precipitation penetration length, $\tilde{L}_C$.

randomly placed nodes. The results are presented in Figure 11, illustrating the pattern variations across different parameter combinations. As before, the simulations are terminated when the system becomes completely clogged or when a breakthrough of a dissolution/precipitation channel occurs. In the former case, the final frame of the simulation presented in Figure 11 is bordered in red (clogging), while in the latter, it is bordered in blue (breakthrough). For a better insight into both the final porosity and the mineral composition of dissolution patterns, two methods of data presentation have been used. Local porosity is presented in Figure 11 by color-coding the pores. The pores with diameters smaller than the initial ones $\left(d^0/10 < d < d^0\right)$ are marked in yellow, while the most overgrown pores $\left(d < d^0/10\right)$ are marked in red. On the other hand, Figure 12 depicts grains enclosed between the pores. Those filled with mineral A are marked in blue, those filled with mineral E are marked in red, while the mixtures of the minerals are marked by various shades of purple. For clarity, yellow is used to mark the empty space in between the grains.

As expected, the ratio of molar volumes of the secondary and primary species, Γ, has a major impact on the patterns by progressively introducing more volume into the system. This affects the overall shape of the channels, which transition from patterns resembling dissolution wormholes at small Γ to tortuous structures with cemented rims at larger Γ values. Eventually, large values of Γ lead to the clogging of the system. However, as discussed in Section 5, even for $\Gamma > 1$, the system can remain permeable, particularly at larger flow rates (smaller Da) and higher initial porosities.

The impact of the reaction rate ratio (κ) on the growing patterns is less obvious. In the low precipitation rate regime, $\kappa = 0.01$ and $\tilde{L}_C = 1$, the system never clogs due to the intense leaching of the C ions from the system, even if $\Gamma > 1$. When Γ is also low (small molar volume of the secondary mineral), the influence of the precipitation reaction becomes negligible, and we obtain dissolution patterns similar to those for pure dissolution (Budek & Szymczak, 2012). However, as we increase Γ, we observe a progressively larger amount of precipitate surrounding the dissolution channel. Since these partially cemented regions are less permeable, their presence hinders side-branching of the wormholes, which become more linear and less fractal. For slightly larger values of the reaction rate ratio ($\kappa = 0.1$), the precipitation occurs closer to the active channel and influences its growth in a more profound way. As shown in Figure 11, the red area of intense overgrowth forms a well-defined conduit inside which a dissolution channel grows. The shape of the conduit defines the subsequent shape of the channel. In some cases (e.g., $\kappa = 0.1, \Gamma = 0.5$), the main channel may even grow backward, opposite to the global pressure gradient, because the area ahead of it is clogged by the precipitate (see Movie S6).

In contrast, for a large precipitation rate, the secondary reaction occurs almost instantaneously, in the immediate neighborhood of where the dissolution takes place. This makes clogging less probable and does not lead to channel bending or branching. Note that as Γ becomes larger, such in situ precipitation results in a decrease in the permeability ratio between dissolution channels and the medium. The reduced permeability ratio changes the way the channels interact with each other. The competition between them becomes weaker, and their shape—less branched but thicker. We can also observe an attraction between shorter channels and their longer neighbors, leading to the formation of loops ($\Gamma = 0.5 - 0.75, \kappa \geq 10$, see Movie S7), which is a characteristic feature of the fingering process in a medium with relatively low mobility contrast between the invading and receding phases (Budek et al., 2017). Note that when $\Gamma \geq 1$, the permeability of the transformed parts becomes equal to or less than that of the surrounding medium. In such cases, the reactive front becomes stable (P. Ortoleva et al., 1987; Szymczak & Ladd, 2014), and the dissolution channels do not form (see e.g., the patterns at $\Gamma = 1$, $\kappa = 100$, where almost all the primary mineral A is replaced by mineral E). Hence, such a system remains homogeneous, and the 1D model of Section 4 is applicable. This means, among other things, that the system will clog beyond $\Gamma^*_{\kappa\to\infty} = \frac{1}{1-\varphi_0}$, as predicted in Section 4.

The most morphologically diverse dissolution patterns are observed for intermediate values of κ and Γ. At these values, $\tilde{L}_C$ is small enough to neglect leakage through the outlet, while the competition between dissolution and precipitation is at its most intense, resulting in numerous thin channels with very short lateral branches (see Movie S8). A particularly intriguing pattern emerges at $\kappa = 1$ and $\Gamma = 0.75$ (see Movie S9), consisting of highly ramified channels with bulbous branches. These branches form due to rapid dissolution, which creates an oval body of the channel, concurrent with equally rapid rim formation that prevents further growth. Eventually, the channel succeeds in dissolving an overpass through the rim and forms a new section of a branch. This process is associated with intense oscillations in system permeability.

The shapes of these channels resemble the patterns that emerge during the slow drainage of a granular-fluid system (Sandnes et al., 2011). In such systems, invading fluid fingers move around the solid grains, building walls around themselves that eventually limit their growth. Here, the mechanism seems to be similar, but with cementation replacing the bulldozing effect.

Now let us examine the morphology of the patterns for a higher initial porosity of the system. Simulation results for $d^0 = 0.3$, $\mathrm{Da} = 0.5$ and wide range of Γ and κ are presented in Figures 13 and 14. In this case dissolution channels for pure dissolution are wider and more diffuse than those for $d^0 = 0.1$. Since more space is available in the system, the range of parameters that lead to the breakthrough is also appreciably wider.

As the initial porosity is larger this time, and the amount of material to be dissolved is smaller, the porosity (and thus also permeability) contrast between dissolution channels and the surrounding medium is weaker than in the previous case. For this reason it is easier to distinguish the channels on the mineral maps of Figure 14 than on the pore diameter maps of Figure 13. A low permeability contrast results in a weaker competition between the growing channels, with more channels remaining active over time. This tendency is additionally strengthened by precipitation, especially for large κ, where it occurs concurrently with dissolution. As a consequence of such a low mobility ratio, we observe loops forming for $\Gamma = 0.1$ and $\kappa \geq 0.1$. For larger molar volumes of E ($\Gamma = 0.5$ and $\Gamma = 0.75$) and $\kappa \geq 1$, dissolution channels begin to merge as the reactive-infiltration instability weakens. When $\Gamma \geq 1$ this process leads to the formation of a uniform front (see Movie S10) with the permeability of the pattern

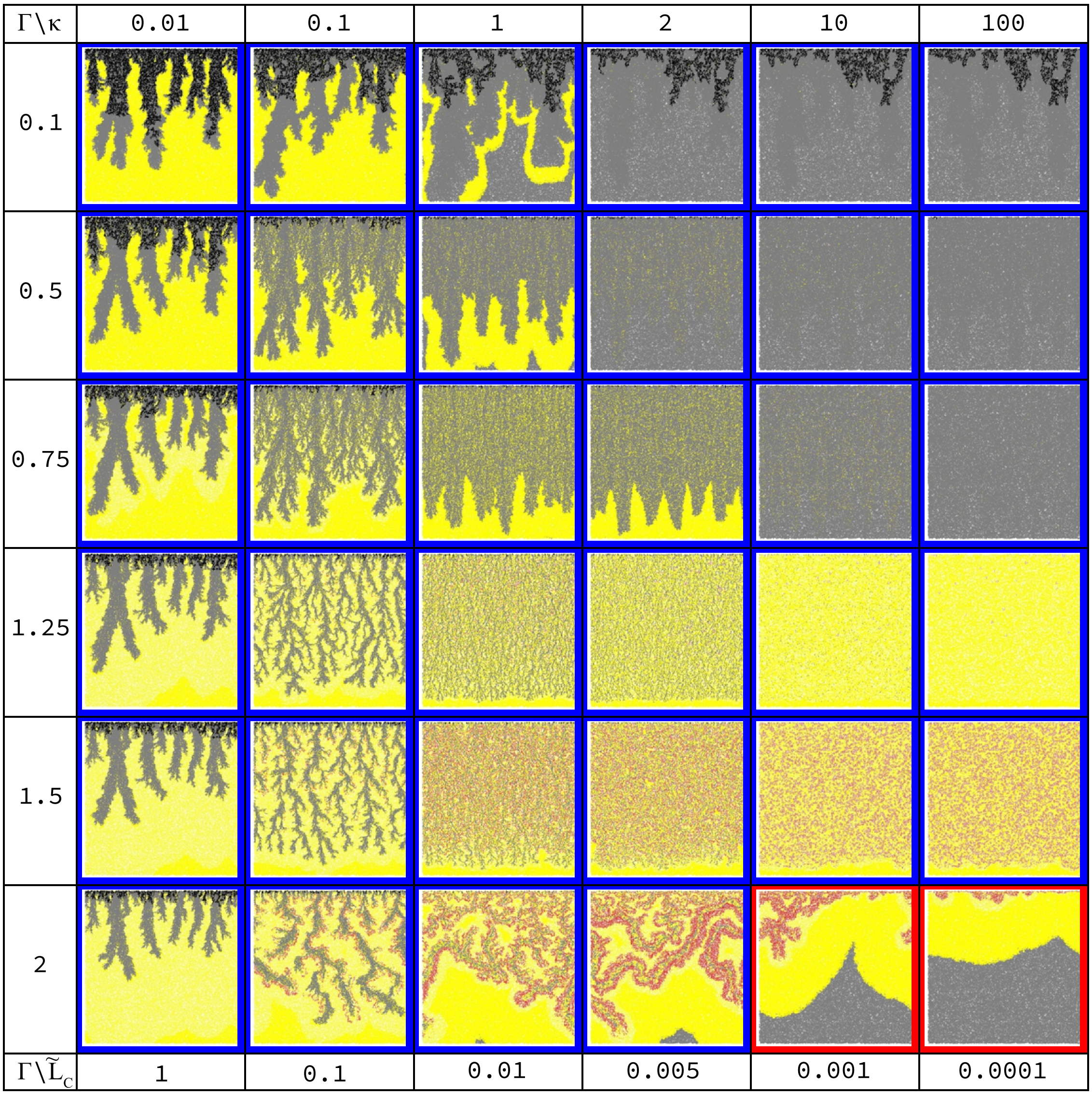

Figure 13. Morphological phase diagram of dissolution-precipitation patterns for various Γ and κ values, with Da = 0.5 and $d^0 = 0.3$ (pore diameter maps). Pores are color-coded as follows: heavily overgrown pores $\left(d \le d^0/10\right)$ are red; intermediate pores $\left(d^0/10 < d \le d^0\right)$ are yellow; pores larger than d^0 but smaller than $2d^0$ $\left(d^0 < d < 2d^0\right)$ are gray; and pores forming the dissolution pattern $\left(d \ge 2d^0\right)$ are black. The lower axis shows corresponding values of the precipitation penetration length, $\tilde{L}_C$.

becoming smaller than that of the initial medium. This time, the uniform front is present for a wider range of precipitation rates ($\kappa \ge 1$) than before. One can also observe that the homogeneity of the system behind the front increases with κ. For intermediate values of κ (e.g., $\kappa = 0.1 - 1$ and $\Gamma = 1.25 - 1.5$), although the front remains flat, there is a dense network of thin, highly branched, and interconnected channels behind it (see Movie S11). For larger κ, these channels merge and are no longer visible, but the porosity of the system remains nonuniform (see Figure 13). At even larger Γ values (e.g., $\Gamma = 2$, $\kappa = 0.1 - 2$), we observe a plethora of branched channels with cemented rims, growing in a tortuous manner as they attempt to bypass clogged regions.

Finally, let us examine dissolution patterns for smaller Da, which corresponds to larger total flow through the system and increased penetration lengths, $\tilde{L}_B$ and $\tilde{L}_C$. The results of the simulations conducted at $d^0 = 0.1$ and $\mathrm{Da} = 0.1$ over a wide range of Γ and κ parameters are presented in Figures 15 and 16. In this case, the channels formed in pure dissolution are wider but not branched (see $\kappa = 0.01$ and $\Gamma = 0.25$). However, the precipitation of secondary species causes these channels to meander significantly in order to bypass overgrown areas (see

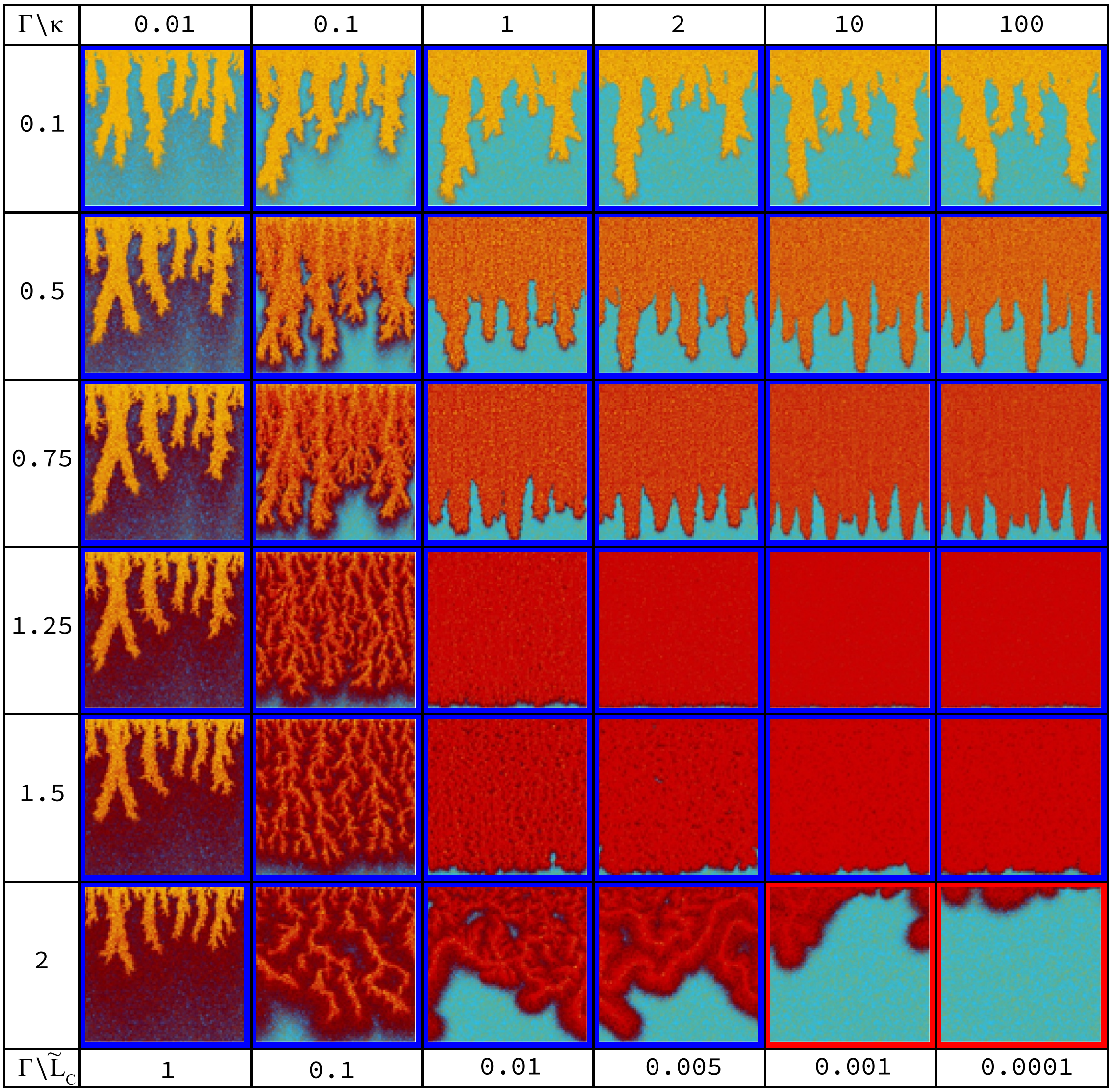

Figure 14. Morphological phase diagram of dissolution-precipitation patterns for various Γ and κ values, with $\mathrm{Da} = 0.5$ and $d^0 = 0.3$ (mineral maps). Colors represent the mineral concentrations within the grains: mineral A is shown in blue, mineral E in red, and mixtures of the two minerals are marked by various shades of purple. Empty space not occupied by grains is marked in yellow. The lower axis shows corresponding values of the precipitation penetration length, $\tilde{L}_C$.

$\kappa = 0.1$). For $\Gamma = 0.75$ and $\kappa = 2$ (see Movie S12), the patterns are the most branched, consisting of nested bulbous shapes. On the other hand, for $\Gamma = 1$ and $\kappa = 10$ (see Movie S13), the results show a lace-like structure of relatively thin and highly branched channels.

Even though the initial porosity is small $\left(d^0 = 0.1\right)$, the longer penetration length makes the system more resistant to clogging, similar to the scenario with $\mathrm{Da} = 0.5$ and $d^0 = 0.3$. On the other hand, the permeability ratio remains high, making the channel merging and a stable front formation possible only for the largest values of $\kappa \geq 100$.

7. Characterization of the Dissolution-Precipitation Patterns

The morphology of dissolution-precipitation patterns clearly changes with the parameters describing the precipitation reaction—κ and Γ, with the latter parameter appearing to have the strongest influence. To capture the morphological diversity of the observed patterns, let us now attempt a quantitative description.

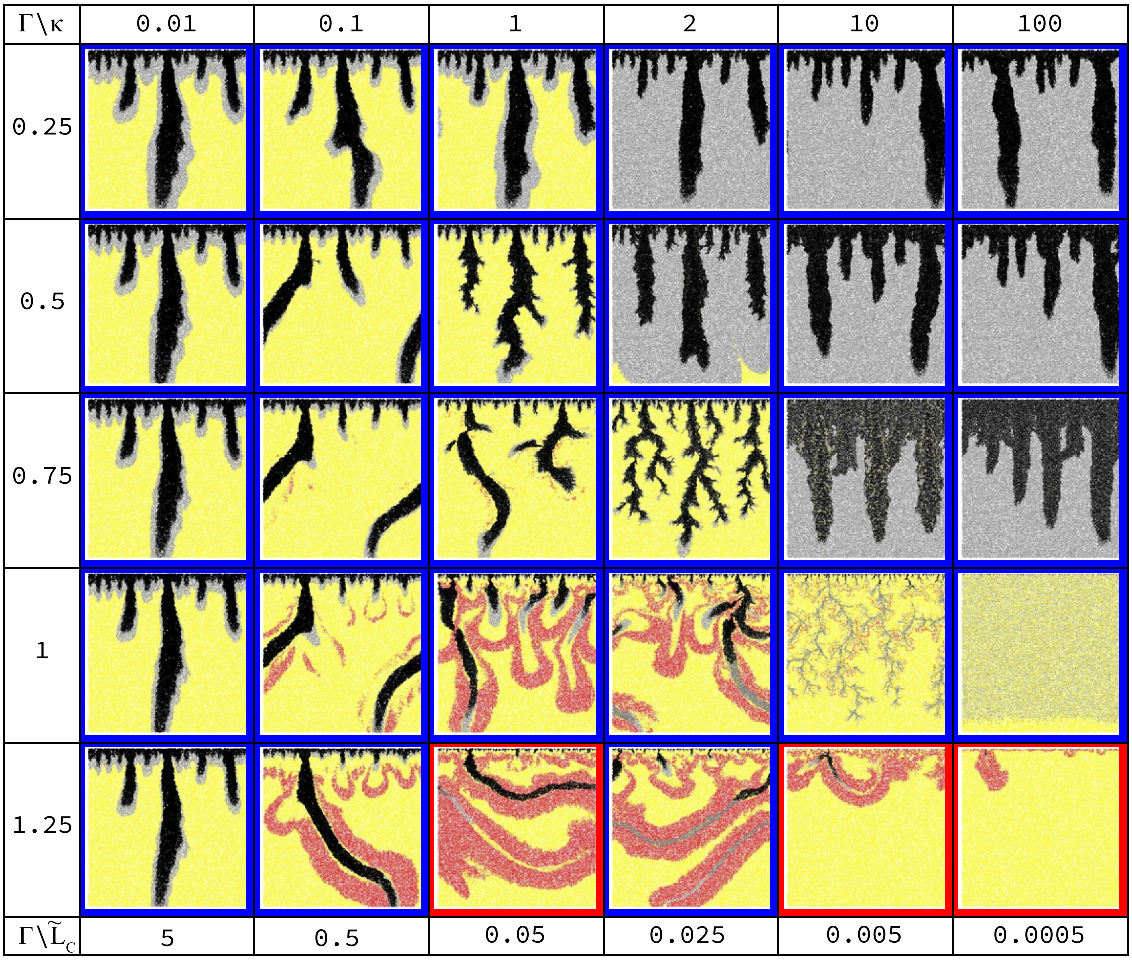

Figure 15. Morphological phase diagram of dissolution-precipitation patterns for various Γ and κ values, with Da = 0.1 and $d^0 = 0.1$ (pore diameter maps). Pores are color-coded as follows: heavily overgrown pores $\left(d \le d^0/10\right)$ are red; intermediate pores $\left(d^0/10 < d \le d^0\right)$ are yellow; pores larger than d^0 but smaller than $2d^0$ $\left(d^0 < d < 2d^0\right)$ are gray; and pores forming the dissolution pattern $\left(d \ge 2d^0\right)$ are black. The lower axis shows corresponding values of the precipitation penetration length, $\tilde{L}_C$.

We will characterize the replacement efficiency by quantifying the amount of dissolved primary mineral and precipitated secondary mineral. Additionally, we will calculate the geometric parameters of the emerging patterns: their tortuosity and degree of branching (ramification). Figures 17a and 17b display the total change in A and E species in the system as a function of Γ for three different values of $\kappa = 0.2, 0.5, 1$. The data are averaged over 40 realizations on a grid of 100×100 random nodes for Da $= 0.5$ and $d^0 = 0.3$. As before, the simulation is terminated if the system becomes clogged or a breakthrough is achieved.

The total amount of dissolved primary mineral, ΔV^A, and deposited secondary mineral, V_E^{final}, show a non-monotonic dependence on the dissolution-precipitation volume ratio, Γ. For small Γ, ΔV^A and V_E^{final} increase with the molar volume of E. As emphasized earlier, the precipitating mineral reduces the contrast in permeability between dissolution channels and the surrounding matrix, weakening the effect of mutual screening of channels. Numerous, usually highly branched channels remain active for a longer period, contributing to a more efficient removal of the primary mineral. In cases of pure dissolution, the total flow and solvent consumption quickly concentrate in a single channel, leaving the majority of the system untouched, and thus not participating in replacement.

On the other hand, for even larger molar volumes of the precipitant, clogging begins to impede the growth of dissolution channels by increasingly cementing the areas around their tips. As a result, the system again reaches a point where only one channel remains active, but it must meander between the overgrown areas.

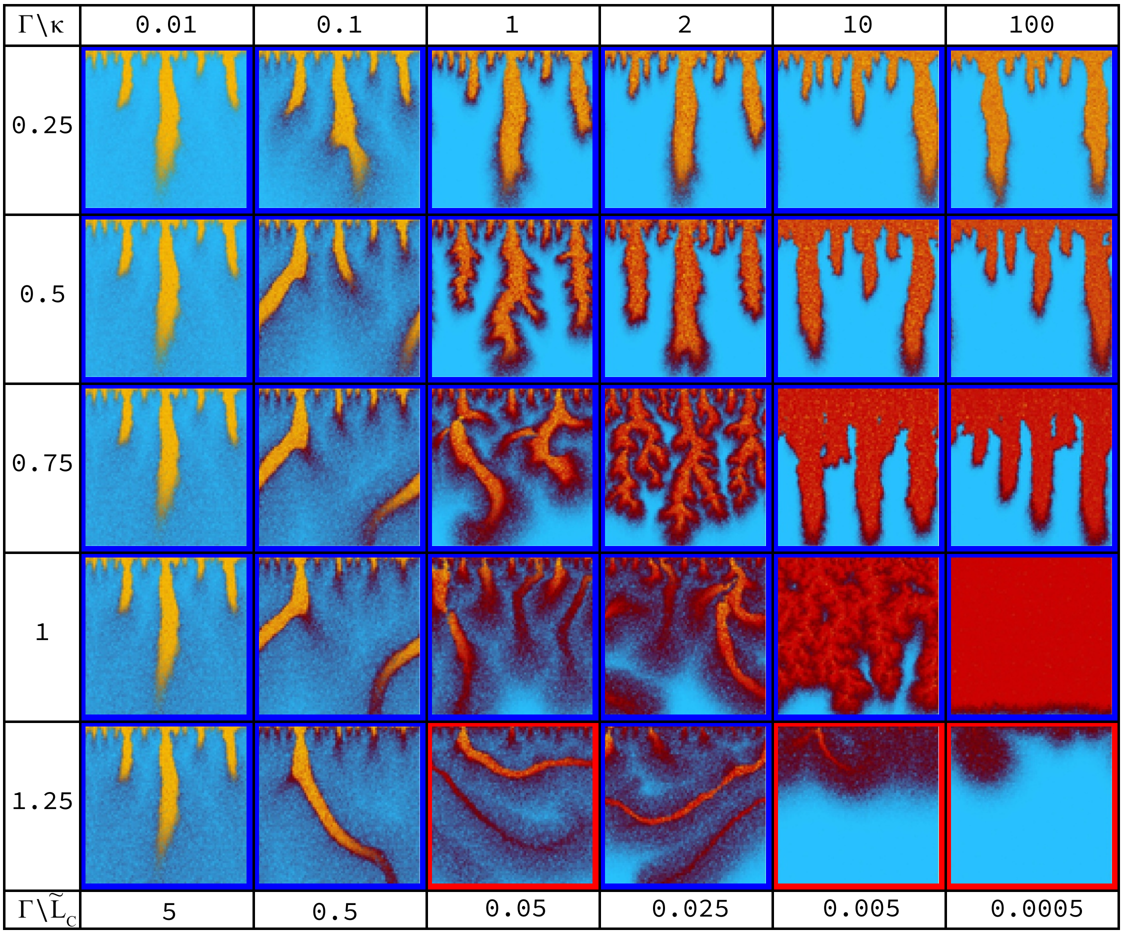

Figure 16. Morphological phase diagram of dissolution-precipitation patterns for various Γ and κ values, with $\mathrm{Da} = 0.1$ and $d^0 = 0.1$ (mineral maps). Colors represent the mineral concentrations within the grains: mineral A is shown in blue, mineral E in red, and mixtures of the two minerals are marked by various shades of purple. Empty space not occupied by grains is marked in yellow. The lower axis shows corresponding values of the precipitation penetration length, $\tilde{L}_C$.

Consequently, for each value of κ, we observe a maximum amount of dissolved material, the height of which, as well as the Γ value at which it occurs, increases with the precipitation rate. Similarly, the total amount of secondary mineral deposited in the system exhibits a pronounced maximum as a function of Γ, with these maxima slightly shifted to the right relative to the maxima of ΔV^A.

In the context of practical applications, it is often important to find conditions which maximize the amount of the secondary mineral precipitated in the system. Figures 18a and 18b show the total volume of E for a wide range of Γ and κ for two different initial porosity values. For $d^0 = 0.1$, the maximal values of V_E^{final} are observed for large κ and Γ close to the critical $\Gamma^*_{\kappa\to\infty} = 1.04$. Note that for $\kappa \to \infty$ and $1 < \Gamma < \Gamma^*$ we expect a stable, uniform front of replacement reaction $\mathrm{A} \to \mathrm{E}$, which maximizes the amount of deposited secondary mineral. Above Γ^*, we expect clogging; thus V_E^{final} decreases sharply with Γ.

For a higher initial porosity, $d^0 = 0.3$, the volume of the secondary mineral increases due to the additional space available in the system for deposition. In the figure, we scale V_E^{final} by the initial volume of the primary mineral, V_A^0, which is smaller at higher initial porosities. This scaling contributes to the higher values of $V_E^{\mathrm{final}}/V_A^0$ observed in the plot. Next, for $d^0 = 0.3$ the critical Γ increases to $\Gamma^*_{\kappa\to\infty} = 1.48$, shifting the maximum of V_E^{final} to a region of larger Γ compared to the case with $d^0 = 0.1$. Finally, because clogging is more difficult to achieve in a porous system, V_E^{final} decreases less sharply above Γ^*.

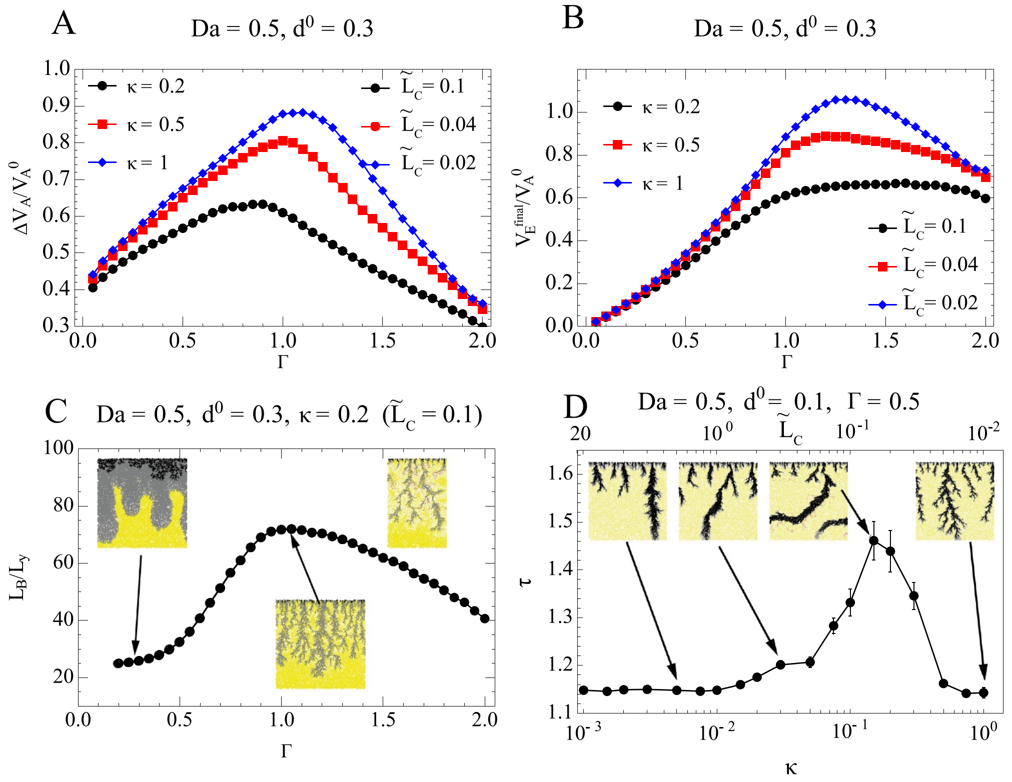

Figure 17. (a) Volume change of mineral A due to dissolution, ΔV_A, normalized by the initial volume, V_A^0, as a function of Γ for Da $= 0.5$ and $d^0 = 0.3$ and three values of κ (0.2, 0.5, 1). The corresponding values of the precipitation penetration length, $\tilde{L}_C$, are also marked. (b) Volume of the deposited secondary mineral, ΔV_E, as a function of Γ for the same parameter values as in (a). (c) Ramification rate as a function of Γ for Da $= 0.5$ and $\kappa = 0.2$. (d) Tortuosity of the dominant wormhole as a function of κ (lower axis) or, alternatively, the precipitation penetration length, $\tilde{L}_C$ (upper axis) for $\Gamma = 0.5$.

The above results were obtained for a Damköhler number of Da = 0.5. Figure 18c explores the effects of varying this value, as well as Γ, while keeping $\kappa = 1$ and $d^0 = 0.1$ fixed. For large Da, wormholing concentrates flow and, consequently, precipitation into relatively thin channels, whereas at small Da, most of the coupling ions, C, are flushed out of the system as $\tilde{L}_C$ becomes large. As a result, we observe a non-monotonic relationship between V_E^{final} and Da, with a single maximum for a given Γ, and an overall maximum at Da $= 0.2$ and $\Gamma = 0.8$.

Let us now turn to the characterization of the geometry of the emergent dissolution channels. As we recall, such a pattern is defined as a set of pores whose diameters have increased by at least a factor of two, $d \geq 2d^0$, and are connected to the system's inlet through other pores that meet this condition. These pores, along with the corresponding nodes where they connect, form a graph, $\mathcal{G}$. We then find the minimum spanning tree of the graph $\mathcal{G}$, which is a subset of edges that connects all the nodes without any cycles and with the minimum possible total edge length. In cases where multiple parallel dissolution channels develop in the system, we will focus on analyzing the dominant one—the channel closest to the outlet—along with its corresponding minimum spanning tree.

The tortuosity of a dissolution channel is then defined as the shortest distance between the inlet and the tip of the longest channel, measured along the minimum spanning tree, normalized by the length of the system. The tortuosity of a dissolution channel as a function of κ for $\Gamma = 0.5$, Da $= 0.5$, and $d^0 = 0.1$ is presented in Figure 17d. The precipitation penetration length, $\tilde{L}_C \sim 1/\kappa$, has a strong impact on the channel shape. For large $\tilde{L}_C$ (small κ), the majority of the precipitant is flushed out of the system, and the pattern resembles the pure dissolution one. When the penetration length is smaller, $\tilde{L}_C \simeq 0.1$, the precipitant forces dissolution channels to meander around overgrown regions, making the tortuosity significantly larger. For the largest κ, when the penetration length is of the order of l^0, the channels become highly branched, although the tortuosity of the main flow path decreases.

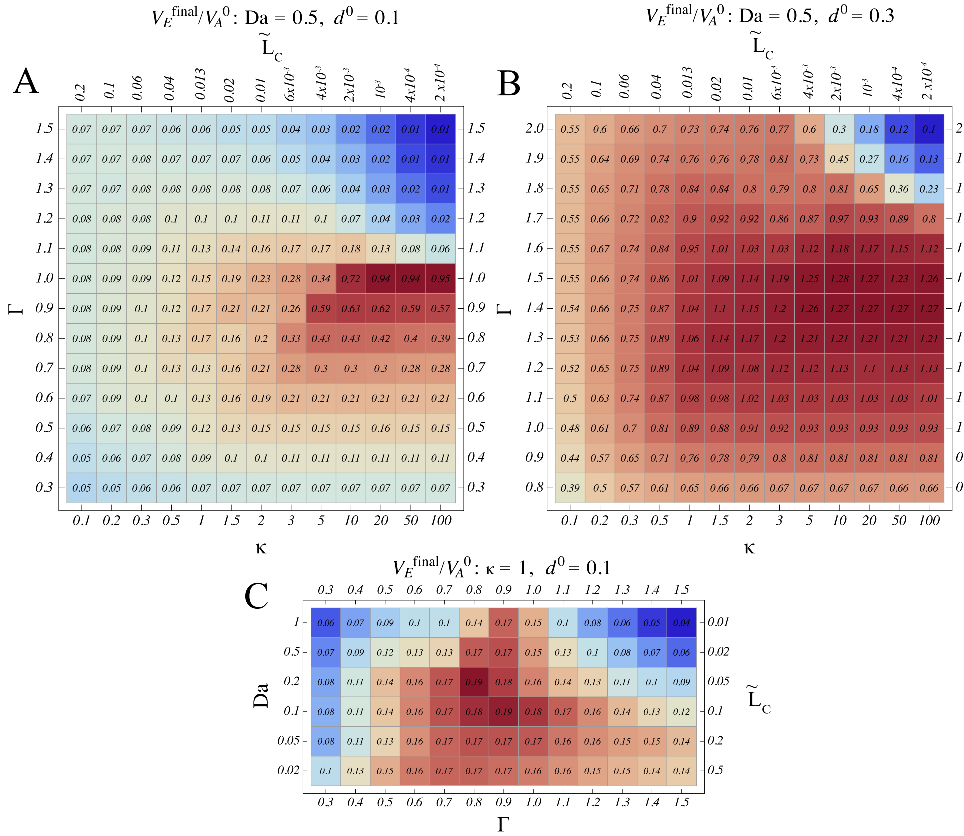

A

$\tilde{L}_C$	0.2	0.1	0.06	0.04	0.013	0.02	0.01	6x10⁻³	4x10⁻³	2x10⁻³	10⁻³	4x10⁻⁴	2 x10⁻⁴
Γ \ κ	0.1	0.2	0.3	0.5	1	1.5	2	3	5	10	20	50	100
1.5	0.07	0.07	0.07	0.06	0.06	0.05	0.05	0.04	0.03	0.02	0.02	0.01	0.01
1.4	0.07	0.07	0.08	0.07	0.07	0.07	0.06	0.05	0.04	0.03	0.02	0.01	0.01
1.3	0.07	0.07	0.08	0.08	0.08	0.08	0.08	0.07	0.06	0.04	0.03	0.02	0.01
1.2	0.08	0.08	0.08	0.1	0.1	0.1	0.11	0.11	0.1	0.07	0.04	0.03	0.02
1.1	0.08	0.08	0.09	0.11	0.13	0.14	0.16	0.17	0.17	0.18	0.13	0.08	0.06
1.0	0.08	0.09	0.09	0.12	0.15	0.19	0.23	0.28	0.34	0.72	0.94	0.94	0.95
0.9	0.08	0.09	0.1	0.12	0.17	0.21	0.21	0.26	0.59	0.63	0.62	0.59	0.57
0.8	0.08	0.09	0.1	0.13	0.17	0.16	0.2	0.33	0.43	0.43	0.42	0.4	0.39
0.7	0.08	0.09	0.1	0.13	0.13	0.16	0.21	0.28	0.3	0.3	0.3	0.28	0.28
0.6	0.07	0.09	0.1	0.1	0.13	0.16	0.19	0.21	0.21	0.21	0.21	0.21	0.21
0.5	0.06	0.07	0.08	0.09	0.12	0.13	0.15	0.15	0.15	0.15	0.16	0.15	0.15
0.4	0.05	0.06	0.07	0.08	0.09	0.1	0.1	0.11	0.11	0.11	0.11	0.11	0.11
0.3	0.05	0.05	0.06	0.06	0.07	0.07	0.07	0.07	0.07	0.07	0.07	0.07	0.07

B

$\tilde{L}_C$	0.2	0.1	0.06	0.04	0.013	0.02	0.01	6x10⁻³	4x10⁻³	2x10⁻³	10⁻³	4x10⁻⁴	2 x10⁻⁴
Γ \ κ	0.1	0.2	0.3	0.5	1	1.5	2	3	5	10	20	50	100
2.0	0.55	0.6	0.66	0.7	0.73	0.74	0.76	0.77	0.6	0.3	0.18	0.12	0.1
1.9	0.55	0.64	0.69	0.74	0.76	0.76	0.78	0.81	0.73	0.45	0.27	0.16	0.13
1.8	0.55	0.65	0.71	0.78	0.84	0.84	0.8	0.79	0.8	0.81	0.65	0.36	0.23
1.7	0.55	0.66	0.72	0.82	0.9	0.92	0.92	0.86	0.87	0.97	0.93	0.89	0.8
1.6	0.55	0.67	0.74	0.84	0.95	1.01	1.03	1.03	1.12	1.18	1.17	1.15	1.12
1.5	0.55	0.66	0.74	0.86	1.01	1.09	1.14	1.19	1.25	1.28	1.27	1.23	1.26
1.4	0.54	0.66	0.75	0.87	1.04	1.1	1.15	1.2	1.26	1.27	1.27	1.27	1.27
1.3	0.53	0.66	0.75	0.89	1.06	1.14	1.17	1.2	1.21	1.21	1.21	1.21	1.21
1.2	0.52	0.65	0.75	0.89	1.04	1.09	1.08	1.12	1.12	1.13	1.1	1.13	1.13
1.1	0.5	0.63	0.74	0.87	0.98	0.98	1.02	1.03	1.03	1.03	1.03	1.03	1.01
1.0	0.48	0.61	0.7	0.81	0.89	0.88	0.91	0.92	0.93	0.93	0.93	0.93	0.93
0.9	0.44	0.57	0.65	0.71	0.76	0.78	0.79	0.8	0.81	0.81	0.81	0.81	0.81
0.8	0.39	0.5	0.57	0.61	0.65	0.66	0.66	0.67	0.67	0.67	0.67	0.66	0.66

C

Da \ Γ	0.3	0.4	0.5	0.6	0.7	0.8	0.9	1.0	1.1	1.2	1.3	1.4	1.5	$\tilde{L}_C$
1	0.06	0.07	0.09	0.1	0.1	0.14	0.17	0.15	0.1	0.08	0.06	0.05	0.04	0.01
0.5	0.07	0.09	0.12	0.13	0.13	0.17	0.17	0.15	0.13	0.1	0.08	0.07	0.06	0.02
0.2	0.08	0.11	0.14	0.16	0.17	0.19	0.18	0.16	0.14	0.13	0.11	0.1	0.09	0.05
0.1	0.08	0.11	0.14	0.16	0.17	0.18	0.19	0.18	0.17	0.16	0.14	0.13	0.12	0.1
0.05	0.08	0.11	0.13	0.16	0.17	0.17	0.17	0.17	0.16	0.16	0.15	0.15	0.14	0.2
0.02	0.1	0.13	0.15	0.16	0.17	0.17	0.17	0.16	0.16	0.15	0.15	0.14	0.14	0.5

Figure 18. (a) Total volume of the precipitated secondary mineral, V_E^{final}, normalized by the initial volume of the primary mineral $\left(V_A^0\right)$ as a function of the molar volume ratio (Γ) and the rate constant ratio (κ, lower axis) or, alternatively, the precipitation penetration length, $\tilde{L}_C$ (upper axis) for Da $= 0.5$ and $d^0 = 0.1$. (b) The same as in (a) but for $d^0 = 0.3$. (c) Total volume of the precipitated secondary mineral, V_E^{final}, normalized by the initial volume of the primary mineral $\left(V_A^0\right)$ as a function of the molar volume ratio (Γ) and the Damköhler number (left axis) or the precipitate penetration length, $\tilde{L}_C$ (right axis).

Finally, we measure the ramification rate by calculating the total circumference of a branched pattern normalized by the length of the system, L. Results are depicted in Figure 17c, where the ramification is presented as a function of Γ for $\kappa = 0.2$, Da $= 0.5$ and $d^0 = 0.3$. When precipitation has little impact on the pattern (small Γ), thick, diffusive channels form without side branches, characterized by a low ramification rate. For stronger precipitation, highly branched channels appear that compete with each other, with ramification peaking at $\Gamma \sim 1$. At the largest Γ values, the massive amount of precipitate hinders channel growth, reducing the number of channels. Although the channels tend to bend, their ramification rate declines.

8. Summary and Conclusions

This study has systematically explored the complex interactions between dissolution and precipitation processes within porous media, using a pore network model. Our investigations reveal that the dynamic balance between these processes can significantly influence the macroscopic properties of the media, such as permeability and structural integrity.

We demonstrated that different regimes of dissolution and precipitation can lead to a variety of morphological outcomes, from channel formation to complete system clogging. Key factors influencing these outcomes include the molar volumes of reactants and products, the relative rates of dissolution and precipitation, and the initial porosity of the medium. Particularly, our results show that the interplay between dissolution and precipitation could lead to the continuous formation of new flow paths and spatial separation of dissolution-dominated and precipitation-dominated regions. In such cases, the system can remain permeable even if the secondary phase has a larger volume than the primary one. Continuously generated flow paths are very efficient in distributing the secondary phase almost uniformly throughout the system.

Several limitations of this study should be acknowledged. First, as mentioned previously, we employ simplified geochemistry in our dissolution-precipitation model. Both reactions were considered irreversible and linearly dependent on reactant concentrations (c_B for dissolution and c_C for precipitation). While this assumption is common in studies of reactive transport instabilities (Chadam et al., 1986; Steefel & Lasaga, 1990) and aligns with our goal to isolate the interplay between flow, dissolution, and precipitation in a minimal model framework, a more general treatment would consider the overall reaction rates as a balance between forward and backward reactions. In natural systems, equilibrium thresholds and fluid composition changes (e.g., pH evolution) may lead to dissolution of secondary phases, altering long-term permeability. Such dynamics could produce cyclical pore clogging and reopening—phenomena not captured by our current model.

Additionally, we have assumed a timescale separation between geometry evolution and flow/transport relaxation times. This enables the quasi-static approach, where flow and concentration fields are treated as stationary at each timestep. However, this assumption breaks down when fluid consumption is substantial (e.g., in serpentinization) requiring future model extensions that incorporate fluid sink terms.

Finally, to keep the model mathematically tractable, we assumed that the changes in the pore volume coming from dissolution/precipitation are distributed uniformly along the pore diameter. While this simplification facilitates calculations, it might overestimate the time required for clogging. In reality, clogging would begin at specific locations within the pore where the precipitation rate is highest. There are also several other important processes not captured by our current framework. The model is deliberately minimalistic, assuming that both primary and secondary mineral reactive areas are simply proportional to the lateral surface of the pore. It neglects the processes such as nucleation of the secondary phase on the primary one, but also the possible lamination of a dissolving mineral by a precipitating one, which can substantially modify the effective reactive surface over time, especially if a passivating layer forms and blocks further interaction between the aqueous phase and the mineral substrate. In future work, incorporating these processes will be central to the development of a more realistic pore-network model. We plan to enrich the description of dissolution and precipitation kinetics by explicitly accounting for nucleation barriers, the emergence of passivation layers, and their effects on the accessibility of pore surfaces. These additions will help capture a broader range of geochemical scenarios and improve the predictive power of the model for long-term dynamics.

Building on these refinements, future work should also focus on extending the simulations to more complex and heterogeneous systems, incorporating a broader range of chemical reactions and physical conditions. This should provide a more detailed understanding of coupled chemical and physical changes in rock evolution and enhance the model applicability to both natural and engineered porous media.

Appendix A: Clogging Conditions for the 1D Model

To determine the condition for clogging in terms of κ and Γ, we consider an effective, Darcy-scale description of our system. Let us consider medium of initial porosity φ_0 infiltrated by a reactive fluid of Darcy velocity u_0 and reactant concentration c_B^{in}. This one-dimensional, continuous system can then be described by the following equations

$$\begin{array}{ll} u_0 \dfrac{\partial c_B(x,t)}{\partial x} = -\theta(v_A)\, k_1 s c_B & u_0 \dfrac{\partial c_C(x,t)}{\partial x} = \theta(v_A)\, k_1 s c_B - k_2 s c_C \\ \dfrac{\partial v_A(x,t)}{\partial t} = -k_1 \chi_A v_A c_B \theta(v_A) & \dfrac{\partial v_E(x,t)}{\partial t} = k_2 \chi_E v_E c_C \end{array}, \tag{A1}$$

where s stands for the specific reactive surface area. The respective boundary conditions are $c_B(x \to -\infty) = c_B^{\text{in}}, c_C(x \to -\infty) = 0$, while the initial conditions are $v_A(t = 0) = v_A^0$ and $v_E(t = 0) = 0$.

Although the full solution of these equations is complicated, even in one dimension, we can consider the long-time limit where all concentration profiles propagate steadily with a constant velocity U, and are thus dependent only on the variable $\xi = x - Ut$.

Under these conditions, the concentration and mineral volume profiles can be found analytically under certain simplifying assumptions. First, we assume that the specific reaction area, s, remains constant during the reaction. Note that, in our model, the surface area does not change significantly over a wide range of porosity values (see Figure 5). Second, we neglect the effects of diffusive hindering (Equation 5). If we choose the origin of coordinates such that for $\xi \le 0$, mineral A has been fully dissolved, we have $c_B(\xi \le 0) = c_B^{\text{in}}$, $c_C(\xi \le 0) = 0$, $v_A(\xi \le 0) = 0$, and $v_E(\xi \le 0) = v_E^{\text{final}}$, where v_E^{final} is the final volume fraction of the secondary mineral attained after the reaction front has passed. On the other hand, for $\xi > 0$, the concentration and volume profiles are:

$$\begin{aligned} c_B &= c_B^{\text{in}} e^{-\frac{sk_1}{u_0}\xi} & \qquad c_C &= \frac{c_B^{\text{in}}}{1-\kappa}\left(e^{-\kappa\frac{sk_1}{u_0}\xi} - e^{-\frac{sk_1}{u_0}\xi}\right) \\ v_A &= v_A^0\left(1 - e^{-\frac{sk_1}{u_0}\xi}\right) & \qquad v_E &= \frac{v_E^{\text{final}}}{1-\kappa}\left(e^{-\kappa\frac{sk_1}{u_0}\xi} - \kappa e^{-\frac{sk_1}{u_0}\xi}\right) \end{aligned}. \tag{A2}$$

Additionally, from mass conservation we find the link between the final volume fraction of the secondary mineral and initial volume fraction of the primary mineral, $v_E^{\text{final}} = \Gamma v_A^0$ as well as the formula for the front propagation velocity, $U = \frac{1}{v_E^{\text{final}}}\chi_A \nu_A c_B^{\text{in}} u_0$. The porosity in the system, $\varphi = 1 - v_A - v_E$, can then be calculated as

$$\varphi(\xi) = \begin{cases} \Gamma\varphi_0 + 1 - \Gamma & \text{for } \xi \le 0 \\ \varphi_0 - (1-\varphi_0)\left(\Gamma\dfrac{\left(e^{-\kappa\frac{sk_1}{u_0}\xi} - \kappa e^{-\frac{sk_1}{u_0}\xi}\right)}{1-\kappa} - e^{-\frac{sk_1}{u_0}\xi}\right) & \text{for } \xi > 0 \end{cases}, \tag{A3}$$

where $\varphi_0 = 1 - v_A^0$ is the initial porosity. The porosity has a single minimum for $\xi = \frac{u_0}{sk_1}\log\left(\frac{(\Gamma-1)\kappa+1}{\Gamma\kappa}\right)/(1-\kappa)$ with the corresponding minimum value

$$\varphi^* = \varphi_0 - (1-\varphi_0)\left(\Gamma\left(\frac{(\Gamma-1)\kappa+1}{\Gamma\kappa}\right)^{\frac{\kappa}{\kappa-1}}\right). \tag{A4}$$

The system avoids clogging if the minimum porosity, φ^*, remains greater than zero ($\varphi^* > 0$). This requirement imposes a condition on the initial porosity, φ_0, expressed in terms of Γ and κ

$$\Gamma\left(\frac{(\Gamma-1)\kappa+1}{\Gamma\kappa}\right)^{\frac{\kappa}{\kappa-1}} < \frac{\varphi_0}{1-\varphi_0}. \tag{A5}$$

which is Equation 25 in the main text.

This condition ensures that the system remains permeable, preventing the porosity from reaching critically low values that could lead to clogging.

Notation

q_{ij}	Flow rate through pore ij $\left[\text{L}^3\text{T}^{-1}\right]$
μ	Fluid viscosity $\left[\text{ML}^{-1}\text{T}^{-1}\right]$
l_{ij}	Length of pore ij [L]
d_{ij}	Diameter of pore ij [L]
p_i	Pressure at node i $\left[\text{ML}^{-1}\text{T}^{-2}\right]$
c_i	Concentration of species i $\left[\text{NL}^{-3}\right]$

Δt	Time step length [T]
χ_i	Stoichiometric coefficient [dimensionless]
k_i	Reaction rate constant for species i $\left[\mathrm{LT}^{-1}\right]$
D_i	Diffusion coefficient of species i $\left[\mathrm{L}^2\mathrm{T}^{-1}\right]$
Sh	Sherwood number [dimensionless]
k^{eff}	Effective reaction rate $\left[\mathrm{LT}^{-1}\right]$
Da_i	Effective Damköhler number for reaction i [dimensionless]
ν_i	Molar volume of species i $\left[\mathrm{L}^3\mathrm{N}^{-1}\right]$
ΔV_{ij}^k	Volume change of reactant k in pore ij $\left[\mathrm{L}^3\right]$
d^0	Initial pore diameter [L]
l^0	Mean pore length [L]
Γ	Ratio of molar volume of precipitating to dissolving species [dimensionless]
κ	Ratio of precipitation to dissolution reaction rates [dimensionless]
V_{ijk}	Volume of grain ijk $\left[\mathrm{L}^3\right]$
V_{ijk}^0	Maximum volume of grain ijk $\left[\mathrm{L}^3\right]$
s	Reactive specific surface area $\left[\mathrm{L}^{-1}\right]$
φ	Porosity [dimensionless]
φ_0	Initial porosity [dimensionless]
L	System length [L]
L_B	Penetration length of species B [L]
L_C	Penetration length of species C [L]
τ	Tortuosity [dimensionless]

Data Availability Statement

All the data produced as a part of this research are available in Budek and Szymczak (2025).

Acknowledgments

This work was supported by the National Science Centre (NCN; Poland) under research Grant 2022/47/B/ST3/03395. Part of this material is based upon work supported by the U.S. Department of Energy, Office of Science, Office of Basic Energy Sciences, Chemical Sciences, Geosciences, and Biosciences Division under Award Number DE-SC0018676. We thank Peter Kelemen and Marc Spiegelman (Lamont-Doherty Earth Observatory of Columbia University) for their insightful comments on the manuscript. We also acknowledge discussions with Peter K. Kang (University of Minnesota).

References

Aharonov, E., Whitehead, J., Kelemen, P., & Spiegelman, M. (1995). Channeling instability of upwelling melt in the mantle. *Journal of Geophysical Research*, *100*(B10), 433–455. https://doi.org/10.1029/95jb01307

Al-Khulaifi, Y., Lin, Q., Blunt, M. J., & Bijeljic, B. (2019). Pore-scale dissolution by CO_2 saturated brine in a multimineral carbonate at reservoir conditions: Impact of physical and chemical heterogeneity. *Water Resources Research*, *55*(4), 3171–3193. https://doi.org/10.1029/2018wr024137

Ameri, A., Raoof, A., Blonk, N., & Cnudde, V. (2017). Detailed modeling of carbonate acidizing by coupling a multi-purpose pore-network simulator to the chemistry package PHREEQC-application to chelating agents. In *SPE Latin America and Caribbean Petroleum Engineering Conference*. SPE-185532-MS. https://doi.org/10.2118/185532-MS

Amestoy, P. R., Duff, I. S., Koster, J., & L'Excellent, J.-Y. (2001). A fully asynchronous multifrontal solver using distributed dynamic scheduling. *SIAM Journal on Matrix Analysis and Applications*, *23*(1), 15–41. https://doi.org/10.1137/s0895479899358194

Amestoy, P. R., Guermouche, A., L'Excellent, J.-Y., & Pralet, S. (2006). Hybrid scheduling for the parallel solution of linear systems. *Parallel Computing*, *32*(2), 136–156. https://doi.org/10.1016/j.parco.2005.07.004

Andreani, M., Luquot, L., Gouze, P., Godard, M., Hoise, E., & Gibert, B. (2009). Experimental study of carbon sequestration reactions controlled by the percolation of CO_2-rich brine through peridotites. *Environmental Science & Technology*, *43*(4), 1226–1231. https://doi.org/10.1021/es8018429

Banerjee, A., & Merino, E. (2011). Terra Rossa genesis by replacement of limestone by kaolinite. III. Dynamic quantitative model. *The Journal of Geology*, *119*(3), 259–274. https://doi.org/10.1086/659146

Barnes, I., O'Neil, J. R., & Trescases, J. (1978). Present day serpentinization in New Caledonia, Oman and Yugoslavia. *Geochimica et Cosmochimica Acta*, *42*(1), 144–145. https://doi.org/10.1016/0016-7037(78)90225-9

Beinlich, A., John, T., Vrijmoed, J. C., Tominaga, M., Magna, T., & Podladchikov, Y. Y. (2020). Instantaneous rock transformations in the deep crust driven by reactive fluid flow. *Nature Geoscience*, *13*(4), 307–311. https://doi.org/10.1038/s41561-020-0554-9

Bejan, A. (1984). *Convection heat transfer*. Wiley.

Budek, A., Kwiatkowski, K., & Szymczak, P. (2017). Effect of mobility ratio on interaction between the fingers in unstable growth processes. *Physical Review E—Statistical Physics, Plasmas, Fluids, and Related Interdisciplinary Topics*, *96*(4), 042218. https://doi.org/10.1103/physreve.96.042218

Budek, A., & Szymczak, P. (2012). Network models of dissolution of porous media. *Physical Review E—Statistical Physics, Plasmas, Fluids, and Related Interdisciplinary Topics*, *86*(5), 056318. https://doi.org/10.1103/physreve.86.056318

Budek, A., & Szymczak, P. (2025). Channeling, clogging and permeability oscillations: Different macroscopic regimes in mineral replacement [Dataset]. *FigShare*. https://doi.org/10.6084/m9.figshare.28235813

Bustillo, M. A. (2010). Silicification of continental carbonates. In *Carbonates in continental settings: Geochemistry, diagenesis and applications* (Vol. 62, pp. 153–178). Elsevier. https://doi.org/10.1016/S0070-4571(09)06203-7

Centrella, S., Beaudoin, N. E., Derluyn, H., Motte, G., Hoareau, G., Lanari, P., et al. (2021). Micro-scale chemical and physical patterns in an interface of hydrothermal dolomitization reveals the governing transport mechanisms in nature: Case of the Layens anticline, Pyrenees, France. *Sedimentology*, *68*(2), 834–854. https://doi.org/10.1111/sed.12808

Chadam, D., Hoff, D., Merino, E., Ortoleva, P., & Sen, A. (1986). Reactive infiltration instabilities. *Journal of Applied Mathematics*, *36*(3), 207–221. https://doi.org/10.1093/imamat/36.3.207

Cochepin, B., Trotignon, L., Bildstein, O., Steefel, C. I., Lagneau, V., & Van der lee, J. (2008). Approaches to modelling coupled flow and reaction in a 2d cementation experiment. *Advances in Water Resources*, *31*(12), 1540–1551. https://doi.org/10.1016/j.advwatres.2008.05.007

Cohen, A., Grayevsky, R., Israeli, Y., & Emmanuel, S. (2021). Coupled dissolution-precipitation reactions as a potential method for mitigating contaminant transport in carbonate aquifers. *Advances in Water Resources*, *157*, 104052. https://doi.org/10.1016/j.advwatres.2021.104052

Cohen, C., Ding, D., Quintard, M., & Bazin, B. (2008). From pore scale to wellbore scale: Impact of geometry on wormhole growth in carbonate acidization. *Chemical Engineering and Science*, *63*(12), 3088–3099. https://doi.org/10.1016/j.ces.2008.03.021

Daccord, G. (1987). Chemical dissolution of a porous medium by a reactive fluid. *Physical Review Letters*, *58*(5), 479–482. https://doi.org/10.1103/physrevlett.58.479

Daccord, G., & Lenormand, R. (1987). Fractal patterns from chemical dissolution. *Nature*, *325*(6099), 41–43. https://doi.org/10.1038/325041a0

Daines, M. J., & Kohlstedt, D. L. (1994). The transition from porous to channelized flow due to melt/rock reaction during melt migration. *Geophysical Research Letters*, *21*(2), 145–148. https://doi.org/10.1029/93gl03052

De Windt, L., Pellegrini, D., & Van Der Lee, J. (2004). Coupled modeling of cement/claystone interactions and radionuclide migration. *Journal of Contaminant Hydrology*, *68*(3–4), 165–182. https://doi.org/10.1016/s0169-7722(03)00148-7

Dewynne, J. N., Fowler, A. C., & Hagan, P. S. (1993). Multiple reaction fronts in the oxidation/reduction of iron-rich uranium ores. *SIAM Journal on Applied Mathematics*, *53*(4), 971–989. https://doi.org/10.1137/0153048

Dreybrodt, W. (1988). *Processes in Karst systems: Physics, chemistry, and geology*. Springer-Verlag.

Economides, M. J., & Nolte, K. G. (2000). *Reservoir stimulation*. John Wiley and Sons.

Ewers, R. O. (1982). *Cavern development in the dimensions of length and breadth*. (Unpublished Doctoral Dissertation). McMaster University.

Garcia-Rios, M., Luquot, L., Soler, J. M., & Cama, J. (2015). Influence of the flow rate on dissolution and precipitation features during percolation of CO_2-rich sulfate solutions through fractured limestone samples. *Chemical Geology*, *414*, 95–108. https://doi.org/10.1016/j.chemgeo.2015.09.005

Golfier, F., Zarcone, C., Bazin, B., Lenormand, R., Lasseux, D., & Quintard, M. (2002). On the ability of a Darcy-scale model to capture wormhole formation during the dissolution of a porous medium. *Journal of Fluid Mechanics*, *457*, 213–254. https://doi.org/10.1017/s0022112002007735

Gupta, N., & Balakotaiah, V. (2001). Heat and mass transfer coefficients in catalytic monoliths. *Chemical Engineering and Science*, *56*(16), 4771–4786. https://doi.org/10.1016/s0009-2509(01)00134-8

Hinch, E. J., & Bhatt, B. S. (1990). Stability of an acid front moving through porous rock. *Journal of Fluid Mechanics*, *212*(-1), 279–288. https://doi.org/10.1017/s0022112090001963

Hoefner, M. L., & Fogler, H. S. (1988). Pore evolution and channel formation during flow and reaction in porous media. *AIChE Journal*, *34*(1), 45–54. https://doi.org/10.1002/aic.690340107

Kelemen, P., Whitehead, J., Aharonov, E., & Jordahl, K. (1995). Experiments on flow focusing in soluble porous media, with applications to melt extraction from the mantle. *Journal of Geophysical Research*, *100*(B1), 475–496. https://doi.org/10.1029/94jb02544

Koeshidayatullah, A., Corlett, H., Stacey, J., Swart, P. K., Boyce, A., & Hollis, C. (2020). Origin and evolution of fault-controlled hydrothermal dolomitization fronts: A new insight. *Earth and Planetary Science Letters*, *541*, 116291. https://doi.org/10.1016/j.epsl.2020.116291

Kondratiuk, P., Tredak, H., Ladd, A. J. C., & Szymczak, P. (2015). Synchronization of dissolution and precipitation fronts during infiltration-driven replacement in porous rocks. *Geophysical Research Letters*, *42*(7), 2244–2252. https://doi.org/10.1002/2015gl063146

Kondratiuk, P., Tredak, H., Upadhyay, V., Ladd, A. J. C., & Szymczak, P. (2017). Instabilities and finger formation in replacement fronts driven by an oversaturated solution. *Journal of Geophysical Research: Solid Earth*, *122*(8), 5972–5991. https://doi.org/10.1002/2017jb014169

Korzhinskii, D. S. (1968). The theory of metasomatic zoning. *Mineralium Deposita*, *231*(3), 222–231. https://doi.org/10.1007/bf00207435

Lasaga, A. C. (1984). Chemical kinetics of water-rock interactions. *Journal of Geophysical Research: Solid Earth*, *89*(B6), 4009–4025. https://doi.org/10.1029/jb089ib06p04009

Li, W., Einstein, H. H., & Germaine, J. T. (2019). An experimental study of matrix dissolution and wormhole formation using gypsum core flood tests: 1. Permeability evolution and wormhole geometry analysis. *Journal of Geophysical Research: Solid Earth*, *124*(11), 11055–11073. https://doi.org/10.1029/2018jb017238

Lichtner, P. C. (1988). The quasi-stationary state approximation to coupled mass transport and fluid-rock interaction in a porous media. *Geochimica et Cosmochimica Acta*, *52*(1), 143–165. https://doi.org/10.1016/0016-7037(88)90063-4

Lipar, M., Szymczak, P., White, S. Q., & Webb, J. A. (2021). Solution pipes and focused vertical water flow: Geomorphology and modelling. *Earth-Science Reviews*, *218*, 103635. https://doi.org/10.1016/j.earscirev.2021.103635

Luquot, L., & Gouze, P. (2009). Experimental determination of porosity and permeability changes induced by injection of CO_2 into carbonate rocks. *Chemical Geology*, *265*(1–2), 148–159. https://doi.org/10.1016/j.chemgeo.2009.03.028

Matter, J. M., & Kelemen, P. B. (2009). Permanent storage of carbon dioxide in geological reservoirs by mineral carbonation. *Nature Geoscience*, *2*(12), 837–841. https://doi.org/10.1038/ngeo683

Menke, H., Reynolds, C., Andrew, M., Nunes, J. P., Bijeljic, B., & Blunt, M. (2018). 4d multi-scale imaging of reactive flow in carbonates: Assessing the impact of heterogeneity on dissolution regimes using streamlines at multiple length scales. *Chemical Geology*, *481*, 27–37. https://doi.org/10.1016/j.chemgeo.2018.01.016

Merino, E., & Canals, A. (2011). Self-accelerating dolomite-for-calcite replacement: Self-organized dynamics of burial dolomitization and associated mineralization. *American Journal of Science*, *311*(7), 572–607. https://doi.org/10.2475/07.2011.01

Noiriel, C., Luquot, L., Madé, B., Raimbault, L., Gouze, P., & van der Lee, J. (2009). Changes in reactive surface area during limestone dissolution: An experimental and modelling study. *Chemical Geology*, *265*, 160–170. https://doi.org/10.1016/j.chemgeo.2009.01.032

Oelkers, E. H., Gislason, S. R., & Matter, J. (2008). Mineral carbonation of CO_2. *Elements*, *4*(5), 333–337. https://doi.org/10.2113/gselements.4.5.333

Ortoleva, P., Chadam, J., Merino, E., & Sen, A. (1987). Geochemical self-organization II: The reactive-infiltration instability. *American Journal of Science*, *287*(10), 1008–1040. https://doi.org/10.2475/ajs.287.10.1008

Ortoleva, P. J. (1994). *Geochemical self-organization*. Oxford University Press.

Ott, H., & Oedai, S. (2015). Wormhole formation and compact dissolution in single-and two-phase CO_2-brine injections. *Geophysical Research Letters*, *42*(7), 2270–2276. https://doi.org/10.1002/2015gl063582

Palmer, A. N. (1991). Origin and morphology of limestone caves. *The Geological Society of America Bulletin*, *103*, 1–21. https://doi.org/10.1130/0016-7606(1991)103<0001:oamolc>2.3.co;2

Panga, M., Ziauddin, M., & Balakotaiah, V. (2005). Two-scale continuum model for simulation of wormhole formation in carbonate acidization. *AIChE Journal*, *51*(12), 3231–3248. https://doi.org/10.1002/aic.10574

Park, Y.-J., de Dreuzy, J.-R., Lee, K.-K., & Berkowitz, B. (2001). Transport and intersection mixing in random fracture networks with power law length distributions. *Water Resources Research*, *37*(10), 2493–2501. https://doi.org/10.1029/2000WR000131

Poonoosamy, J., Kosakowski, G., Van Loon, L. R., & Mäder, U. (2015). Dissolution–precipitation processes in tank experiments for testing numerical models for reactive transport calculations: Experiments and modelling. *Journal of Contaminant Hydrology*, *177*, 1–17. https://doi.org/10.1016/j.jconhyd.2015.02.007

Putnis, A. (2021). Fluid–mineral interactions: Controlling coupled mechanisms of reaction, mass transfer and deformation. *Journal of Petrology*, *62*(12), egab092. https://doi.org/10.1093/petrology/egab092

Raoof, A., Nick, H., Wolterbeek, T., & Spiers, C. (2012). Pore-scale modeling of reactive transport in wellbore cement under CO_2 storage conditions. *International Journal of Greenhouse Gas Control*, *11*, S67–S77. https://doi.org/10.1016/j.ijggc.2012.09.012

Rege, S. D., & Fogler, H. S. (1989). Competition among flow, dissolution, and precipitation in porous media. *AIChE Journal*, *35*(7), 1177–1185. https://doi.org/10.1002/aic.690350713

Roded, R., Aharonov, E., Holtzman, R., & Szymczak, P. (2020). Reactive flow and homogenization in anisotropic media. *Water Resources Research*, *56*(12), e2020WR027518. https://doi.org/10.1029/2020wr027518

Roded, R., Szymczak, P., & Holtzman, R. (2021). Wormholing in anisotropic media: Pore-scale effect on large-scale patterns. *Geophysical Research Letters*, *48*(11), e2021GL093659. https://doi.org/10.1029/2021gl093659

Rowan, G. (1959). Theory of acid treatment of limestone formations. *Journal of the Institute of Petroleum*, *45*(431), 321.

Sandnes, B., Flekkøy, E., Knudsen, H., Måløy, K., & See, H. (2011). Patterns and flow in frictional fluid dynamics. *Nature Communications*, *2*(1), 288. https://doi.org/10.1038/ncomms1289

Sanna, A., Uibu, M., Caramanna, G., Kuusik, R., & Maroto-Valer, M. (2014). A review of mineral carbonation technologies to sequester CO_2. *Chemical Society Reviews*, *43*(23), 8049–8080. https://doi.org/10.1039/c4cs00035h

Sharma, R. P., Deng, J., Kang, P. K., & Szymczak, P. (2023). Effects of mixing at pore intersections on large-scale dissolution patterns and solute transport. *Geophysical Research Letters*, *50*(21), e2023GL105183. https://doi.org/10.1029/2023gl105183

Singurindy, O., & Berkowitz, B. (2003a). Evolution of hydraulic conductivity by precipitation and dissolution in carbonate rock. *Water Resources Research*, *39*(1). https://doi.org/10.1029/2001wr001055

Singurindy, O., & Berkowitz, B. (2003b). Flow, dissolution, and precipitation in dolomite. *Water Resources Research*, *39*(6). https://doi.org/10.1029/2002wr001624

Snippe, J., Berg, S., Ganga, K., Brussee, N., & Gdanski, R. (2020). Experimental and numerical investigation of wormholing during CO_2 storage and water alternating gas injection. *International Journal of Greenhouse Gas Control*, *94*, 102901. https://doi.org/10.1016/j.ijggc.2019.102901

Soulaine, C., Roman, S., Kovscek, A., & Tchelepi, H. A. (2017). Mineral dissolution and wormholing from a pore-scale perspective. *Journal of Fluid Mechanics*, *827*, 457–483. https://doi.org/10.1017/jfm.2017.499

Spiegelman, M., Kelemen, P., & Aharonov, E. (2001). Causes and consequences of flow organization during melt transport: The reaction infiltration instability in compactable media. *Journal of Geophysical Research*, *106*(B2), 2061–2077. https://doi.org/10.1029/2000jb900240

Steefel, C. I., & Lasaga, A. C. (1990). Evolution of dissolution patterns: Permeability change due to coupled flow and reaction. In D. C. Melchior & R. L. Bassett (Eds.), *Chemical modeling of aqueous systems II* (pp. 212–225). American Chemical Society. https://doi.org/10.1021/bk-1990-0416.ch016

Szymczak, P., & Ladd, A. J. C. (2009). Wormhole formation in dissolving fractures. *Journal of Geophysical Research*, *114*(B6), B06203. https://doi.org/10.1029/2008jb006122

Szymczak, P., & Ladd, A. J. C. (2011). The initial stages of cave formation: Beyond the one-dimensional paradigm. *Earth and Planetary Science Letters*, *301*(3–4), 424–432. https://doi.org/10.1016/j.epsl.2010.10.026

Szymczak, P., & Ladd, A. J. C. (2014). Reactive infiltration instabilities in rocks. Part 2. Dissolution of a porous matrix. *Journal of Fluid Mechanics*, *738*, 591–630. https://doi.org/10.1017/jfm.2013.586

Trotignon, L., Didot, A., Bildstein, O., Lagneau, V., & Margerit, Y. (2005). Design of a 2-D cementation experiment in porous medium using numerical simulation. *Oil and Gas Science and Technology*, *60*(2), 307–318. https://doi.org/10.2516/ogst:2005019

Varloteaux, C., Békri, S., & Adler, P. M. (2013). Pore network modelling to determine the transport properties in presence of a reactive fluid: From pore to reservoir scale. *Advances in Water Resources*, *53*, 87–100. https://doi.org/10.1016/j.advwatres.2012.10.004

Wagner, R., Kühn, M., Meyn, V., Pape, H., Vath, U., & Clauser, C. (2005). Numerical simulation of pore space clogging in geothermal reservoirs by precipitation of anhydrite. *International Journal of Rock Mechanics and Mining Sciences*, *42*(7–8), 1070–1081. https://doi.org/10.1016/j.ijrmms.2005.05.008

Wicks, F. J., & Whittaker, E. J. W. (1977). Serpentine textures and serpentinization. *The Canadian Mineralogist*, *15*, 459–478.

Woods, A. (2014). *Flow in porous rocks*. Cambridge University Press.